





The Holocene sedimentary record of Mittie Glacier dynamics in Smith Bay, Ellesmere Island (eastern Canadian Arctic Archipelago)

ELODIE BRACQUART,^{1*}  JEAN-CARLOS MONTERO-SERRANO,¹  PATRICK LAJUNESSE,²  GUILLAUME ST-ONGE¹  and LUKE COPLAND³ 

¹Institut des sciences de la mer (ISMER), Université du Québec à Rimouski (UQAR), Geotop & Québec-Océan, Rimouski, Québec, Canada

²Département de Géographie, Université Laval, Québec-Océan, Québec, Québec, Canada

³Department of Geography, Environment and Geomatics, University of Ottawa, Ottawa, Ontario, Canada

Received 11 March 2025; Revised 19 June 2025; Accepted 16 July 2025

ABSTRACT: The physical, sedimentological, mineralogical, and elemental geochemical properties of sediment cores collected in Smith Bay (22BC and 01PC), and near the front of Mittie Glacier (23BC and 01GC), were used to reconstruct glacial sediment discharge and trace the long-term composition and provenance of detrital sediments for the northeastern part of Manson Icefield, southeast Ellesmere Island, over the last 9.2 cal ka BP. The mineralogical and geochemical signatures of core 01GC support the hypothesis of the gradual opening of Nares Strait between 8.8 and 8.2 cal ka BP and suggest a progressive retreat of glaciers surrounding Smith Bay. Lower sedimentation rates ($<14 \text{ cm ka}^{-1}$) recorded in core 01GC during the Middle Holocene, combined with the presence of coarse-grained sediments, indicate a landward retreat of Mittie Glacier and sea-ice free conditions during summer in Smith Bay from 5.4 to 3 cal ka BP. During the Late Holocene, the deposition of six coarse-grained layers close to Mittie Glacier seems to have been triggered by subglacial lake discharges upstream of its western arm. The only known surge of Mittie Glacier, recorded between 1992 and 2007, is identified in the core 23BC by a marked increase in coarse-grained sediment input. © 2025 The Author(s). *Journal of Quaternary Science* Published by John Wiley & Sons Ltd.

KEYWORDS: glacial marine sedimentation; Holocene climate; lithofacies; Manson Icefield; sediment provenance

Introduction

The Arctic is warming at up to four times the global rate, with some regions warming by $>4^\circ\text{C}$ over the past ~30 years, driving a dramatic reduction in Arctic sea ice and retreat of glaciers (e.g., Serreze and Francis, 2006; Serreze and Barry, 2011; Sharp et al., 2011; Cohen et al., 2014; Huang et al., 2017; IPCC, 2021). The Canadian Arctic Archipelago (CAA), located north of the Canadian mainland, is covered by ice caps and icefields over ~15% of its surface, totaling more than 100 000 km². It is home to nearly 300 marine-terminating glaciers (Sharp et al., 2011; Van Wychen et al., 2020), a significant number of which are found around Manson Icefield (Southeast Ellesmere Island), including Mittie Glacier (Copland et al., 2003). Marine-terminating glaciers, with their front in contact with the ocean, are more sensitive to environmental changes than land-terminating glaciers, as they are influenced by both atmospheric and oceanographic conditions (Cook et al., 2019). However, the response of CAA glaciers to recent warming is spatially variable, with the highest retreat rates observed on smaller ice masses (Thomson et al., 2011; Sharp et al., 2014; White and Copland, 2018). Despite their importance, long-term (>50 years) calving rates and sediment fluxes of CAA marine-terminating glaciers remain poorly documented throughout the Holocene, and the precise mechanisms (whether atmospheric or oceanic) controlling their frontal changes are not well understood (Cook et al., 2019). Therefore, a deeper

understanding of long-term glacial sediment dynamics and the role of atmospheric and oceanic forcing on marine-terminating glaciers in the CAA is essential for predicting future glacier behavior in this polar region.

The configuration and sedimentological structures preserved in sediment deposits near glacier margins reflect past glacier dynamics and can be used to reconstruct their variations and responses to climate and oceanographic drivers during the Holocene (e.g., O'Regan et al., 2021; Stevenard et al., 2022; Rodriguez-Cuicas et al., 2023). In this context, the present study focuses on a set of sediment cores (AMD2103-22BC, -01PC/TWC, -23BC, and -01GC) collected across Smith Bay in summer 2021 (Figs. 1(A) and 2(A)). This bay provides a good location to record temporal variation in glacial sediment discharge from Mittie Glacier and northeastern Manson Icefield beyond the instrumental record, as well as oceanic influences from the West Greenland Current (WGC) and Arctic Surface Water (ASW). A multiproxy approach, including ²¹⁰Pb measurements and radiocarbon dating, along with analyses of physical, sedimentological, mineralogical, and elemental geochemical properties, is combined to: (1) reconstruct the long- and short-term changes in detrital sediment transfer from Mittie Glacier related to climate variability since the last deglaciation; (2) determine how changing climatic and oceanic conditions during the Holocene influenced sediment dynamics in the bay; and (3) assess the significance of recent glaciological changes on northeastern Manson Icefield.

This study complements previous paleoclimate and paleoenvironmental research conducted in northern Baffin Bay (e.g., St-Onge and St-Onge, 2014; Georgiadis et al., 2018; Jennings et al., 2019; Caron et al., 2020; Stevenard et al., 2022;

*Correspondence: Elodie Bracquart, as above.

E-mail: elodie.bracquart@gmail.com

Okuma et al., 2023) and provides new insights into the past dynamics of Mittie Glacier. By analyzing dominant sedimentary processes in Smith Bay, we also refine our understanding of its connection to regional climate history throughout the Holocene.

Regional settings

Geology, oceanography, and climate

Smith Bay is located northeast of Manson Icefield, between Makinson Inlet and Baffin Bay, and is surrounded by multiple marine-terminating glaciers (Harrison et al., 2015). The bedrock geologic units around Smith Bay vary in age from

Archean to Paleozoic (Fig. 1(A); Brown, 1972; Harrison et al., 2015). Bordering Smith Bay and the eastern part of Makinson Inlet, the exposed ice-free areas are Archean to Paleoproterozoic in age. These crystalline shield rocks related to the Ellesmere-Ingfield Mobile Belt are mainly composed of granite, granitoid, and paragneiss, which are rich in quartz, plagioclase, and K-feldspar (Brown, 1972; Harrison et al., 2015). The bedrock on the western side of Makinson Inlet consists of extensive Paleozoic carbonates, siliciclastic rocks, and evaporites, rich in calcite, dolomite, and quartz (Brown, 1972; Harrison et al., 2015). The present-day sediments, namely tills, silts, and clays found around Manson Icefield and on the Smith Bay seafloor, are mainly derived from glacial erosion of surrounding landmasses. These sediments

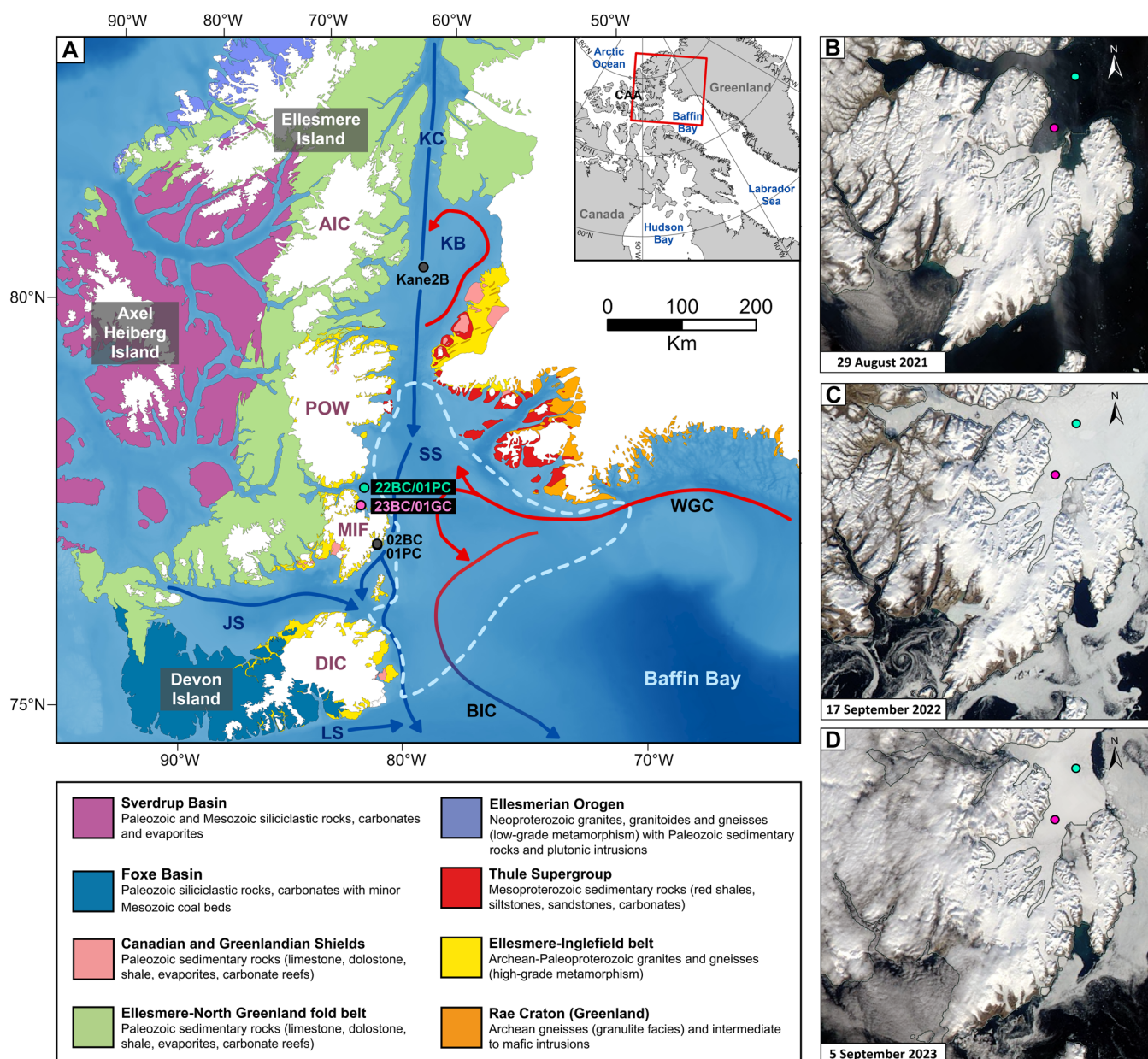


Figure 1. Maps of study area. (A) Topobathymetric (IBCAO; Jakobsson et al., 2020) and geological map (Harrison et al., 2015) of northern Baffin Bay with major surface currents. Red arrows represent warm surface currents ($>2^{\circ}\text{C}$), and blue arrows represent cold Arctic Surface Water (ASW) ($<-1^{\circ}\text{C}$). The blue dashed line represents the NOW (North Water Polynya) area. WGC = West Greenland Current; BIC = Baffin Island Current; LS = Lancaster Sound; JS = Jones Sound; SS = Smith Sound; KB = Kane Basin; KC = Kennedy Channel; MIF = Manson Icefield; POW = Prince of Wales Icefield; DIC = Devon Ice Cap; AIC = Agassiz Ice Cap. Cores studied or cited in this paper are marked by circles: green for 22BC = AMD2103-22BC and 01PC = AMD2103-01PC/TWC, pink for 23BC = AMD2103-23BC and AMD2103-01GC, gray for 02BC = AMD1803-02BC and AMD1803-01PC (Stevenard et al., 2022) and Kane2B = AMD14-Kane2B (Caron et al., 2019, 2020; Georgiadis et al., 2018). MODIS satellite images from (B) 29 August 2021, (C) 17 September 2022, and (D) 5 September 2023 showing snapshots of the sea ice and iceberg distribution around Mittie Glacier (source: NASA Worldview) with the location of cores 22BC-01PC (green circle), 23BC-01GC (pink circle). [Color figure can be viewed at [wileyonlinelibrary.com](https://onlinelibrary.wiley.com/doi/10.1002/jqs.70005)] See the Terms and Conditions (<https://onlinelibrary.wiley.com/terms-and-conditions>) on Wiley Online Library for rules of use. OA articles are governed by the applicable Creative Commons License

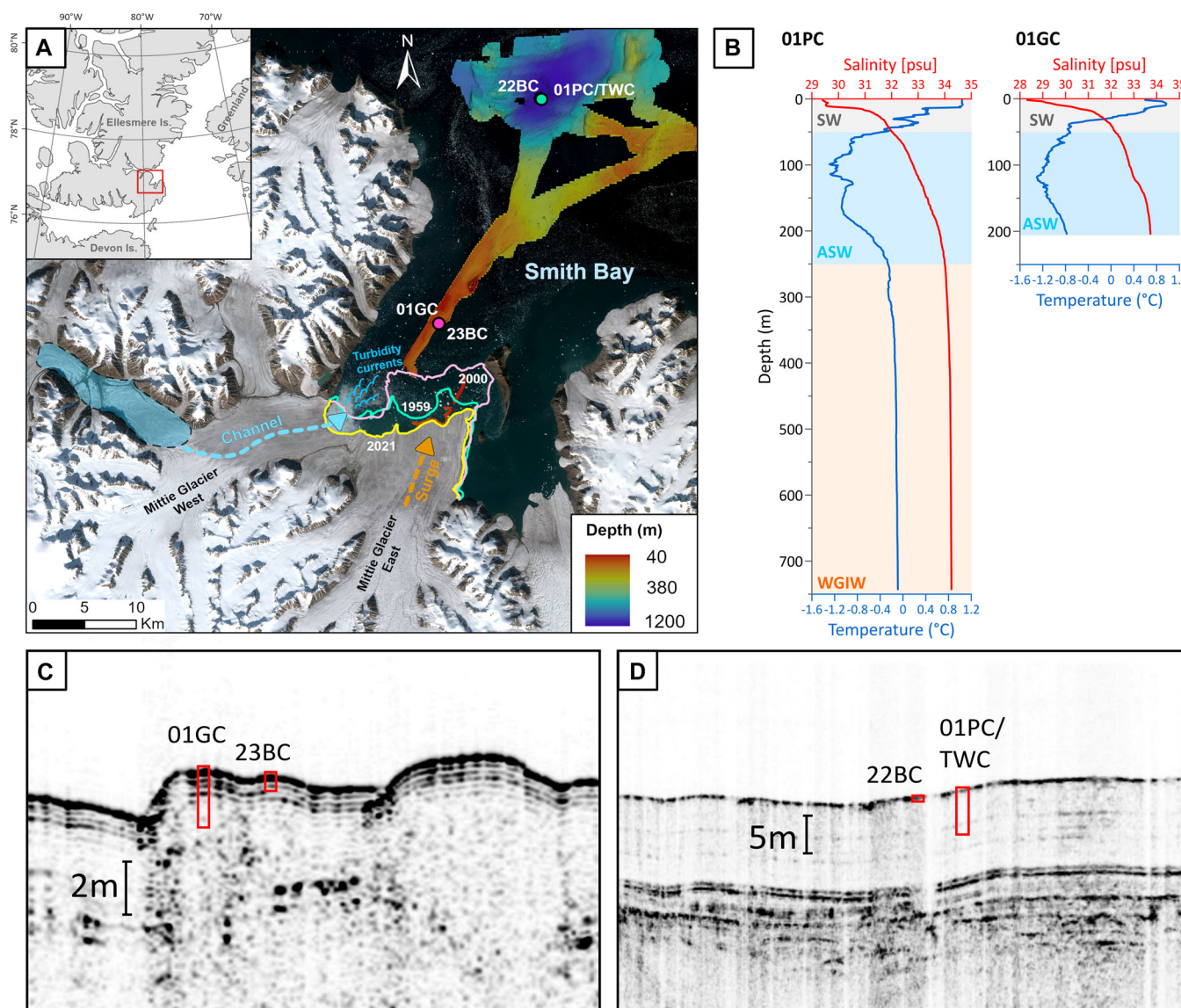


Figure 2. (A) Sentinel-2 satellite image from 23 August 2021 (Source: Nasa Worldview, <https://worldview.earthdata.nasa.gov/>) showing a snapshot of Smith Bay as well as the bathymetry and the location of the cores in this study. The colored lines indicate the positions of the ice margin in 1959 based on air photos from the National Air Photo Library (Ottawa) and in 2000 and 2021 based on satellite imagery acquired by Landsat 7 ETM+ and Landsat 8 OLI sensors downloaded from the United States Geological Survey Earth Explorer (<https://earthexplorer.usgs.gov/>). (B) Temperature and salinity profiles from CTD (conductivity, temperature, and depth) casts taken during the 2021 Amundsen expedition at the core locations of 01PC—Smith Bay (2021-09-02) and 01GC—Mittie Glacier (2021-09-03). SW: Surface Water, ASW: Arctic Surface Water, and WGIW: West Greenland Intermediate Water. (C–D) Sub-bottom profiles at the coring stations in Smith Bay with the position for each core (22BC, 23BC, 01GC, 01PC/TWC). [Color figure can be viewed at [wileyonlinelibrary.com](https://onlinelibrary.wiley.com/terms-and-conditions)]

result from various sedimentary processes, including ice-rafted debris (IRD), glaciogenic debris flows, meltwater plumes, and turbidity currents (e.g., Marlowe, 1966; Hiscott et al., 1989; Ó Cofaigh et al., 2003; Simon et al., 2014; Andrews et al., 2018; Stevenard et al., 2022).

Before 2021, little was known of the bathymetry or oceanography of Smith Bay (Fig. 2(A)–(D)), except for a single multibeam line completed during the 2008 expedition of the CCGS Amundsen (Amundsen Science, 2008). The circulation of water masses in Canadian Arctic fjords is generally controlled by freshwater input, the presence or absence of a bathymetric sill, and sea-ice cover. In Smith Bay (Fig. 2(B)), the temperature-salinity profiles show three layers. A surface layer (SW) dominated by relatively fresh water (and ice) coming from the glacierized landmasses surrounding the bay (Amundsen Science, 2021), the Arctic Surface Water (ASW) from ~50 to 250 m, characterized by cold temperatures (-1.1°C to -0.3°C) and low salinity (33 to 34 psu), and the West Greenland Intermediate Water (WGIW) from ~250 and

743 m, characterized by relatively warm (-0.3°C to -0.8°C) and saline waters (~34 psu). These layers are in accordance with those reported by Sadler (1973) in Makinson Inlet and by Tang et al. (2004) in northern Baffin Bay. Locally, the tidal range impacting glacier fronts in this region has a small amplitude of 1 to 1.20 m (Dunphy et al., 2005; Vincent and Marsden, 2008) and is not believed to have a significant impact on iceberg calving events (Dalton et al., 2019). The swath-bathymetry shows no evidence of a sill at the entrance of the bay, allowing exchange of sea water and quasi-continuous circulation at depth (Fig. 2(A)).

In the area, summers (June–August) are cool and short, with an average temperature of 2.7°C recorded at the Grise Fiord meteorological station in 2023. In contrast, the rest of the year (September–May) is characterized by cold temperatures, averaging -18.6°C in 2023 (<https://climate.weather.gc.ca>). These temperature conditions allow Smith Bay and Makinson Inlet to remain covered by sea ice from September to May. The sea ice typically begins to break up in June, starting from

the outer regions and progressing inward. In recent years (2014–2023, except for 2016 and 2021), the bay remained blocked by coastal ice during July and only began to break up at the end of August (Fig. 1(B)–(D); <https://worldview.earthdata.nasa.gov/>).

Mittie Glacier: a surge-type glacier

Glacier surging describes ice motion variations characterized by cyclical variations, with a long-lived quiescent phase of slow ice flow followed by short-lived active periods of significantly accelerated ice flow (e.g., Meier and Post, 1969; Raymond, 1987; Dowdeswell et al., 1991; Copland et al., 2003). Only ~1% of the world's glaciers have been observed actively surging (Jiskoot et al., 1998; Sevestre and Benn, 2015), with surge-type glaciers seeming to occur within an optimal climatic envelope defined by temperature and precipitation thresholds (Sevestre and Benn, 2015). The highest concentration of surge-type glaciers in the CAA is found in the southeastern part of Ellesmere Island, specifically on Manson Icefield (Copland et al., 2003, 2024). Mittie Glacier (Fig. 2(A)), the largest surge-type glacier in the area, surged between approximately 1992 and 2007 (Copland et al., 2003, 2024; Sharp et al., 2011), advancing >7 km between 1994 and 1999. During this period, the glacier experienced thinning of 10 to 25 m over its lower parts and surface velocities reaching a peak of 4800 m a⁻¹ (Copland et al., 2003, 2024). Today, Mittie Glacier is in a quiescent phase and retreating, with a net area loss of ~2 km² a⁻¹ between 2000 and 2020 (Van Wychen et al., 2014; Kochtitzky and Copland, 2022).

Recently, Gray et al. (2024) identified a 52 km² subglacial lake in an enclosed basin to the west of Mittie Glacier, fed by several converging ice tongues. The glacier surface overlying the lake dropped in elevation by >140 m over a period of ~30 days in early 2021, implying an outburst flood of ~4 km³. Identification of post-outflow crevassing on satellite imagery and height changes on the ASTER Digital Elevation Model show evidence that these subglacial outflows have recurred on an approximately 14-year cycle, with previous drainage events in 1993 and 2007–2008 prior to the most recent one (Gray et al., 2024).

Holocene history in northern Baffin Bay and Nares Strait

From the Last Glacial Maximum to the beginning of the Early Holocene, the Laurentian (LIS), Innuitian (IIS), and Greenland (GrIS) ice sheets (Dyke et al., 2002; England et al., 2006; Dalton et al., 2020) formed a continuous ice belt across the CAA. By expanding into fjord systems and filling major marine channels such as Nares Strait, Smith or Lancaster Sounds (Dyke et al., 2002; Dalton et al., 2020), these ice sheets prevented the influx of Arctic Ocean water and ice into Baffin Bay (Dyke et al., 2002; Knudsen et al., 2008; Jennings et al., 2011; Pieńkowski et al., 2013). Warmer temperatures during the Early Holocene due to high summer insolation

(Laskar et al., 2004) triggered the retreat of the LIS, IIS, and GrIS, leading to a progressive opening of the oceanic connections between the Arctic Ocean and Baffin Bay, beginning with the deglaciation of Lancaster Sound at 13.5 cal ka BP (Dalton et al., 2020; Kelleher et al., 2022; Okuma et al., 2023) and Barrow Strait at 11.5 cal ka BP (Pieńkowski et al., 2012, 2013). The deglaciation progressed from Smith Sound around 11.15 to 10.4 cal ka BP to the north of Nares Strait (Jennings et al., 2011). At 9.0 cal ka BP, Kane and Hall basins opened simultaneously as evidenced by Georgiadis et al. (2018) and Caron et al. (2019, 2020). With the separation of the IIS and the GrIS, the final opening connecting the Arctic Ocean to Baffin Bay occurred in Kennedy Channel between 8.5 and 8.3 cal ka BP (Jennings et al., 2011, 2019; St-Onge and St-Onge, 2014; Georgiadis et al., 2018). Following a decreasing boreal summer insolation, proxy reconstructions show a gradual cooling in air temperatures during the Middle to Late Holocene (Marcott et al., 2013), referred to as Neoglacial cooling that culminated during the Little Ice Age (LIA) and promoted the regrowth of the glaciers across northern Baffin Bay (Kaufman et al., 2009; St-Onge and St-Onge, 2014; Solomina et al., 2015; Briner et al., 2016). Since the end of the 19th century, a rapid increase in air temperatures has caused a recession of most CAA glaciers as well as a reduction in the duration and extent of sea-ice cover (e.g., Miller et al., 2005; Carr et al., 2013; Noël et al., 2018; Cook et al., 2019; Ciraci et al., 2020; Van Wychen et al., 2020; Kochtitzky and Copland, 2022).

Material and methods

Coring and sampling

Sediment cores were recovered in Smith Bay during the 2021 ArcticNet expedition onboard the Canadian Coast Guard Ship (CCGS) icebreaker Amundsen (Fig. 2(A)). Coring sites were determined using high-resolution seismic profiles and swath-bathymetric data to identify areas with continuous Holocene sequences showing no mass movements or sediment perturbations (Fig. 2(C),(D)). Cores AMD2103-22BC (22BC) and AMD2103-01PC/TWC (01PC/TWC) were collected at the entrance of Smith Bay, while cores AMD2103-23BC (23BC) and AMD2103-01GC (01GC) were collected near the front of Mittie Glacier (Table 1). Subsampled 1-cm-wide sections were taken at each centimeter for cores 22BC and 23BC, whereas they were taken at ~4 cm intervals for core 01GC and ~4–8 cm intervals for core 01PC.

Physical and chemical properties

All cores were scanned with a GEOTEK X-CT system to acquire digital X-ray images useful to identify facies and sedimentary structures (St-Onge et al., 2007). The wet bulk density on whole cores was measured at 0.5 cm intervals for cores 22BC, 23BC, 01GC, 01TWC, and at 1 cm intervals for core 01PC, using a GEOTEK Multi-Sensor Core Logger (MSCL).

Table 1. Summary of core stations.

Core ID	Location	Latitude (°N)	Longitude (°W)	Water depth (m)	Core length (cm)	Date of collection (yyyy-mm-dd)
AMD2103-22BC	Smith Bay	77.196	78.590	761	49	2021-09-02
AMD2103-01PC	Smith Bay	77.195	78.586	758	600	2021-09-03
AMD2103-01TWC	Smith Bay	77.195	78.586	758	169	2021-09-03
AMD2103-23BC	Mittie Glacier	76.999	79.016	210	65	2021-09-03
AMD2103-01GC	Mittie Glacier	76.999	79.017	209	227	2021-09-03

BC = box core; GC = gravity core; PC = piston core; TWC = trigger weight core.

The wet bulk density depends significantly on the grain size and mineral composition of sediments and is thus a good indicator for lithological and porosity changes (St-Onge et al., 2007). The cores were then split and visually described, and high-resolution digital color photographic images (HRP) were taken using a GEOTEK Geoscan IV imagery system. Next, the cores were analyzed one more time with the MSCL to measure the low-field volumetric magnetic susceptibilities (k_{LF}), diffuse spectral reflectance parameters, and chemical composition via portable X-ray fluorescence (pXRF) at 0.5 cm intervals for cores 22BC, 23BC, 01GC, 01TWC, and at 1 cm intervals for core 01PC. The diffuse spectral reflectance giving the sediments colors was obtained using a portable Minolta CM-2600d online spectrophotometer coupled to the MSCL. Sediment color is expressed according to the L^* (total reflectance), a^* , b^* color space of the International Commission of Light (e.g., St-Onge et al., 2007). Only the L^* and a^* indexes will be used in this study. L^* ranges from 0 (black) to 100 (white) and a^* from -60 (green) to $+60$ (red) (e.g., St-Onge et al., 2007; Debret et al., 2011). The relative elemental composition (including Al, Si, Ti, Ca, K, Fe, Mn, Zn, Rb, Sr, Zr) of sediment cores was analyzed using an energy-dispersive Olympus Innov-X DELTA pXRF analyzer integrated with the MSCL and equipped with a 40 kV rhodium anode X-ray tube. The pXRF analyzer was calibrated using the Olympus Innov-X standard alloy #316. Elemental concentrations obtained in parts per million (ppm) were subsequently converted to weight percent (wt.%) using the conversion factor 1 wt.% = 10 000 ppm, to facilitate interpretation and visualization.

Quantitative X-ray diffraction mineralogy and sediment sources

The quantitative X-ray diffraction mineralogy (qXRD) of the <2 mm bulk sediment fraction is used to determine the potential sources of sediments and to identify changes in their provenance during the Holocene. The qXRD of the samples was analyzed following the method developed by Eberl (2003). Sample preparation was undertaken by grinding 1 g of dry sediment spiked with 0.25 g of corundum in a McCrone micronizing mill with 5 mL of ethanol for 7 min. The slurry was air-dried overnight before 0.25 mL of Vertrel was added to the mixture to prevent the agglomeration of finer particles. Next, the sample was sieved (<500 μ m), backloaded into the holders, and analyzed on a PANalytical X'Pert Powder diffractometer. The samples were scanned between 5° and 65° two-theta with a step of 0.02° two-theta, and a count time of 2 s per step. The quantification was established by converting the intensity data into mineral weight percentage (wt.%) using the powdR software (Butler and Hillier, 2021). This fitting method allows quantification of the mineralogy in a sample with an average absolute bias of 0.6% for non-clay minerals, 2% for clay minerals, and 5% for amorphous phases (Omotoso et al., 2006; Butler and Hillier, 2021). The principal minerals that were quantified by this method comprise amphibolite (Am), biotite (Bt), calcite (Cal), chlorite (Chl), dolomite (Dol), Fe-bearing (Fe.b; magnetite, hematite), illite (Ill, including muscovite), K-feldspar (Kfs), kaolinite (Kln), plagioclase (Pl), pyroxene (Px), quartz (Qz), smectite (Sme), and vermiculite (Vm). The calculated total mineral wt.% was normalized to a sum of 100%.

To quantitatively assess downcore changes in bulk sediment provenance, we used the nonlinear unmixing Excel macro SedUnMix (Andrews and Eberl, 2012; Andrews et al., 2015, 2016). SedUnMix was run with normalized data for principal minerals that collectively accounted for >85% of the total mineral concentration in the sediment samples. Based on surface geology

(e.g., Brown, 1972; Harrison et al., 2015), sediment transport pathways (e.g., Tang et al., 2004), and recent sediment provenance studies conducted in northern Baffin Bay (e.g., Andrews et al., 2015, 2018; Jennings et al., 2019, 2022; Caron et al., 2020; Stevenard et al., 2022), we propose that Late Quaternary sediments near Mittie Glacier and Smith Bay represent a mixture of two primary source areas: (1) Ellesmere-Inglefield Mobile Belt characterized by plagioclase and feldspar-dominated sediments (Stevenard et al., 2022); and (2) eastern Ellesmere Island, where detrital carbonates, primarily calcite and dolomite, dominate (Bicera-Nfundiko, 2024).

Grain size analysis

Grain size analyses (<2 mm fraction) were performed at 1 cm resolution in cores 22BC and 23BC and ~1–4 cm resolution in cores 01PC/TWC and 01GC using a Malvern-Panalytical Mastersizer 3000 particle-size analyzer equipped with a Hydro LV module and following the instrumental conditions outlined in Belzile and Montero-Serrano (2022). Samples were pretreated with 10 mL of hydrogen peroxide (H_2O_2 ; 30%) to remove organic matter and isolate the detrital fraction of the sediment, diluted with ~20 mL of Calgon solution (1% sodium hexametaphosphate), sieved at <2 mm, and disaggregated using an in-house rotator for 12 h prior to analysis. The grain size composition (clay, silt, and sand) and statistics (e.g., D_{90}) were processed using the GRADISTAT software version 9.1 (Blott and Pye, 2001). The sortable silt mean size (\overline{SS}), corresponding to the mean grain-size of the noncohesive silt fraction (10–63 μ m) and the percentage of sortable silt (SS%) in the <63 μ m fraction, was calculated following the method described in McCave and Andrews (2019a) to provide insight into sediment transport by near-bottom currents. In addition, the IRD abundance was quantified by counting the gravel-sized clasts >2 mm on the X-CT scans of the cores in contiguous 2-cm windows (Grobe, 1987).

Chronology

The chronology of the sediment cores 01PC and 01GC was constrained by eight accelerator mass spectrometry (AMS) radiocarbon (^{14}C) ages (Table 2). A total of seven shell samples were analyzed at the A.E. Lalonde AMS laboratory (University of Ottawa, Canada), while a small quantity of mixed benthic foraminifera sample was analyzed using a Mini-Carbon-Dating-System (MICADAS) at the Alfred Wegener Institute—Helmholtz Center for Polar and Marine Research (Bremerhaven, Germany). Based on a recently published revised regional marine reservoir correction (ΔR) values from Arctic North America for the Marine20 calibration curve (Pearce et al., 2023), the resulting ^{14}C ages were calibrated using the Marine20 data set (Heaton et al., 2020) with a ΔR of 71 ± 69 years (Table 2). This ΔR considers the confluence of AW and the WGS in Smith Bay, which has different ΔR values. The chronology of short sediment cores (22BC and 23BC) was assessed by ^{210}Pb measurements (Table S1). Before the analysis, sediment samples were sieved through a 150- μ m Nitex® mesh, oven-dried (60°C), and crushed and homogenized with an agate mortar. The sediment samples were sieved to prevent biases in ^{210}Pb data linked to bulk grain size variations. ^{210}Pb measurements were performed at the Geotop Research Center (Montréal, Canada) by alpha spectrometry (Ghaleb, 2009).

Age modeling

Box and trigger weight corers are designed to recover a relatively undisturbed sample of the sediment–water interface.

Table 2. Accelerator mass spectroscopy (AMS) radiocarbon dates and calibration for cores 01PC and 01GC.

Laboratory number	Core	Material	Depth in core (cm)	¹⁴ C age (yr BP)	$\Delta R = 71 \pm 69$ cal yr BP	
					Median probability	Range 2σ
12381.1.1**	01GC	Mixed-benthic foraminifera	120–124	3129 \pm 60	2755	2501–3063
UOC-21665	01GC	Mollusc shell (<i>Macoma calcaria</i>)	200.5–202.5	8243 \pm 18	8410	8199–8595
UOC-21666	01GC	Mollusc shell (<i>Macoma calcaria</i>)	218–219	8541 \pm 18	8920	8692–9158
UOC-22237	01PC	Shell fragment	266	4130 \pm 19	3553	3522–3956
UOC-21670	01PC	Gastropod fragment	375	4942 \pm 15	4880	4709–5042
UOC-21671	01PC	Shell fragment	416–417	5225 \pm 16	5243	5077–5392
UOC-21672	01PC	Shell fragment	470	5552 \pm 16	5638	5491–5796
UOC-21673	01PC	Shell fragment	572	6088 \pm 17	6368	6203–6575

The ages were calibrated using rbacon and the Marine20 calibration curve.**Sample analyzed with a Mini-Carbon-Dating-System (MICADAS) at the Alfred Wegener Institute (Bremerhaven, Germany).

Thus, we estimated the absence and deformation of sediments at the tops of the piston and gravity cores based on the correlation of k_{LF} and b^* profiles for cores 22BC and 01PC/TWC and of k_{LF} and $\ln(Fe/Ca)$ profiles for cores 23BC and 01GC (Fig. S1). These correlations suggest a slight compaction at the top of core 01PC, with no material lost during coring. In contrast, about 15 cm of sediments are missing in the upper part of core 01GC, with deformations due to compaction during coring. Therefore, 22BC-01PC/TWC and 23BC-01GC were combined, respectively, into two composite sequences: 01SBCS and 01MCS. The upper 32 cm of core 01SBCS corresponds to core 22BC, and the rest of the sequence corresponds to core 01PC (32–612 cm). In core 01MCS, the upper 51 cm corresponds to core 23BC, and the rest corresponds to core 01GC (51–256.5 cm). The age-depth models were generated using the corrected composite depths.

The Short-Lived Radionuclide Chronology (SERAC) R package and the Constant Flux Constant Sedimentation (CFCS) model—assuming no mixing or Pb diffusion in the sediment (Bruel and Sabatier, 2020)—were used to construct the ²¹⁰Pb-based age model for cores 22BC and 23BC. These results, combined with radiocarbon dating, were then processed using the R package “rbacon” (version 3.3.1; Blaauw and Christen, 2011) to generate the most robust age-depth model for the composite sequences 01SBCS and 01MCS. The rbacon package estimates the best-fit (or weighted mean) age for each depth with a 95% confidence interval using a Bayesian approach.

Results and interpretation

Geochemical and mineralogical characteristics

A boxplot of the major element compositions (pXRF) of bulk sediments for all cores is dominated by Si (~0.5%–15%), Al (~0.3%–2.8%), K (~0.3%–3%), Ca (~0.7%–10.3%), Ti (~0.09%–0.9%) and Fe (~3.7%–7.2%) while Mn, Rb, Sr, Zr, and Zn show lower concentrations (<0.1%) (Fig. 3(A)). Furthermore, the boxplot of qXRD data of the overall bulk sediment fraction illustrates that cores are dominated by Pl (11%–39%), Kfs (10%–22%), Qz (8%–21%), Cal+Dol (0%–28%), Bt+Chl (5%–17%), Sme (0%–17%), Ill+Ms (2%–17%) and Vm (0%–9%), and by lower proportions (<5%) of Am, Px, Fe-b minerals, and Kln (Fig. 3(B)). In general, Pl, Kfs, Qz, Cal+Dol, Bt+Chl, Sme, Ill+Ms, and Vm represent >90% of the overall mineral concentration in all sediment cores. The ternary plot Pl+Kfs–Cal+Dol–Bt+Chl and the boxplots indicate that, in general, cores located closer to Mittie Glacier (23BC and 01GC) contain higher proportions of

Pl, Kfs, Qz, Bt+Chl, and Px, whereas cores farther into Smith Bay (22BC and 01PC) exhibit higher proportions in Cal+Dol, Sme, Ill+Ms, Vm, Am and Kln (Fig. 3(B),(C)). Although slight variations exist in mineral proportions, the main sediment source comes from the Ellesmere–Ingfield Mobile Belt. However, at the base of core 01GC (216–225 cm), analysis of the IRD fraction (>2 mm) shows that the dominant source was Eastern Ellesmere Island carbonates (Figs. 3(C) and 5).

Grain size distribution and sortable silt

The grain size distributions indicate that the cores are dominated by fine-grained sediments consisting of silts and clays (~94%), with some intervals composed of medium to coarse sand (Figs. 4 and 5). The vertical profiles of D_{90} in the sediment cores show mean values ranging from 35 to 63 μ m, with the highest values, 297 μ m and 264 μ m, found in cores 23BC and 01GC, respectively (Fig. 5). A good positive coefficient of correlation between \overline{SS} and $SS\%$, including intervals composed of medium to coarse sand, was obtained for all the cores ($r = 0.72$, $n = 49$ for 22BC; $r = 0.85$, $n = 149$ for 01PC; $r = 0.78$, $n = 65$ for 23BC; $r = 0.90$, $n = 85$ for 01GC). In the cores, up to 86% of the data exhibit a five-point running downcore correlation (r_{run}) greater than 0.5 between \overline{SS} and $SS\%$, suggesting that the sortable silt record is generally well sorted by bottom currents (Fig. S2). Exceptions occur in intervals dominated by medium to coarse sand, particularly at the top of cores 23BC and 01GC, where current sorting is less reliable. These findings support the use of the sortable silt record as a proxy for bottom current strength in Smith Bay area.

Sedimentary lithofacies

Five sedimentary lithofacies (LF; Figs. 4, 5, 7, S3 and S4) were identified in ice-distal (Smith Bay; LFSB) and ice-proximal (Mittie Glacier; LFM) sediment cores based on visual core descriptions, high-resolution core imagery, X-CT scan images, physical and geochemical properties, grain size parameters, and mineralogical data.

Ice-distal settings (cores 22BC and 01PC)

LFSB1 (600–230 cm; 6.6 to 3.2 cal ka BP), recognized in the lower part of core 01PC, is an olive brown (2.5Y 4/3) silty mud with few disseminated gravel-sized clasts (Fig. 4). Slight bioturbation and a few pyritized microfaunal burrows can be observed. Two subunits are recognized, separated by a transition from higher to lower values of k_{LF} , a^* , $\ln(Ca/K)$, and $\ln(Zr/Rb)$, and by a continuous increase in D_{90} and \overline{SS} values. LFSB1a (600–440 cm) is marked by the presence of

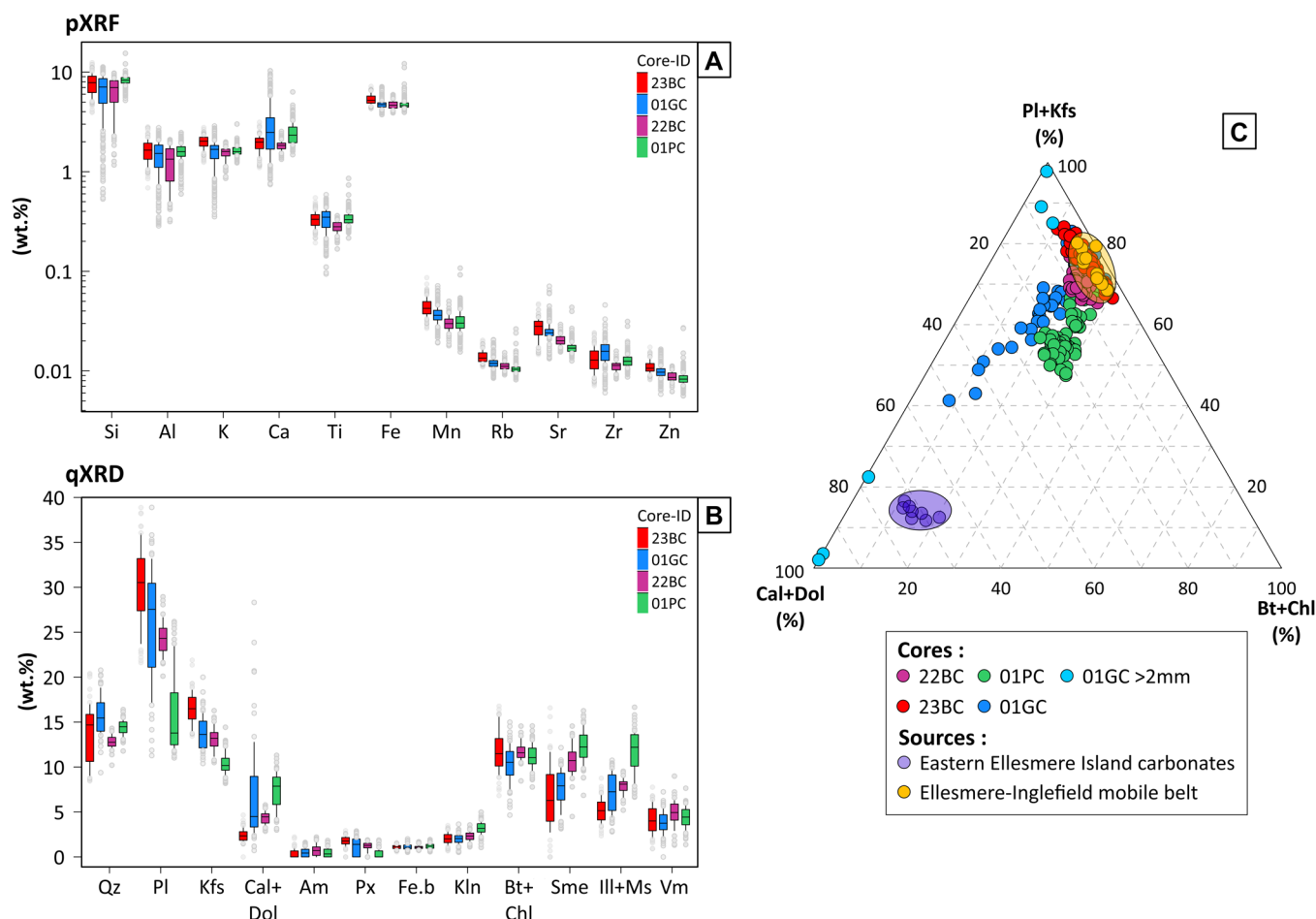


Figure 3. (A) Boxplot of the chemical (pXRF) distribution of the main elements (wt.%) within the cores. (B) Boxplot of the mineralogical distribution of the main minerals (wt.%) within the cores. Note that the relative concentrations obtained with the pXRF sensor were converted to percentage (1% = 10 000 ppm) for better visualization. (C) Mineralogical ternary plot of Plagioclase + K-feldspar (Pl+Kfs) – Biotite + Chlorite (Bt+Chl) – Calcite + Dolomite (Cal+Dol). Eastern Ellesmere Island carbonates data are from Bicara-Nfundiko (2024), and Ellesmere-Inglefield Mobile Belt data are from Stevenard et al. (2022). [Color figure can be viewed at [wileyonlinelibrary.com](https://onlinelibrary.wiley.com/doi/10.1002/jqs.70005)]

planar light-colored centimeter-scale laminae and pyritized microfaunal burrows only visible on the X-CT scans (Fig. 4). Few laminations are enriched in Ca, as shown by a punctual increase in $\ln(\text{Ca}/\text{K})$. In LFSB1b (440–230 cm), the millimeter to centimeter-scale laminations disappear, the grain size percent shows a slight increase in coarse silt and sand, but little to no variation in all the detrital proxies is observed. The provenance of the sediments is half originating from Ellesmere-Inglefield Mobile Belt and half originating from Eastern Ellesmere Island carbonates. Overall, LFSB1 seems to record a period influenced by meltwater outwash dominated by suspension settling in an ice-distal environment (O'Regan et al., 2021).

LFSB2 (core 01PC: 230–0 cm, core 22BC: 49–0 cm; 3.2 cal ka BP to present day) is an olive brown (2.5Y 4/3) silty mud with disseminated gravel-sized clasts interpreted as IRD (Fig. 4). In this lithofacies, an increase in the k_{LF} , a^* , and the percentage of Pl+Kfs is correlated with a decrease in D_{90} , \overline{SS} , $\ln(\text{Zr}/\text{Rb})$, $\ln(\text{Ca}/\text{K})$ values, and the percentage of Cal+Dol (Fig. 4). Both cores show decreased k_{LF} values at the top, likely due to higher water contents (~60%) in the sediments. The sedimentary sources reverse and become mainly derived from Manson Icefield around 160 cm (~2.1 cal ka BP). The percentage of sand and D_{90} show higher values between 220 and 150 cm, before decreasing steadily towards the top of the cores (Fig. 4). In core 01PC, the amount of IRDs suddenly increases to around 115 cm and remains high to the top of the core; a quite large quantity of IRD is also observed in core 22BC. Additionally, in core 01PC, two pluri-centimetric

granitic rocks can be seen on the HRP and X-CT scans at approximately 215–218 cm and 114–125 cm (Fig. 4). The variations observed in the interval between 230 and 150 cm suggest a distal glacial marine setting influenced by meltwater outwash and sea-ice rafting (e.g., Powell, 1981; Stevenard et al., 2022). An increase in fine silt-sized particles and Pl content, along with the appearance of redder lithologies in the upper 150 cm of the unit, indicates enhanced delivery of rock-flour-rich meltwater from the Manson Icefield into Smith Bay. These changes suggest intensified subglacial erosion and meltwater discharge (e.g., Dowdeswell et al., 2015; Stevenard et al., 2022; Rodríguez-Cuicas et al., 2023). The uppermost sediments are also characterized by a heterogeneous assemblage of coarse clasts within a finer-grained matrix, consistent with increased IRD deposition during episodic calving from the marine-terminating margin of the Manson Icefield. Together, these sedimentological features reflect a dynamic glacial regime characterized by both meltwater discharge and episodic iceberg calving.

Ice-proximal setting (cores 23BC and 01GC)

LFM1 (225–200 cm; 9.2 to 8.4 cal ka BP) is an olive brown layer (2.5Y 4/3) consisting of clast-rich silty to sandy diamict as evidenced by the X-CT scans, the IRD count, and the grain size percentage (Fig. 5). The \overline{SS} profile displays consistently low values (~22 μm), indicating stable near-bottom current intensity. This lithofacies displays the highest values of the detrital

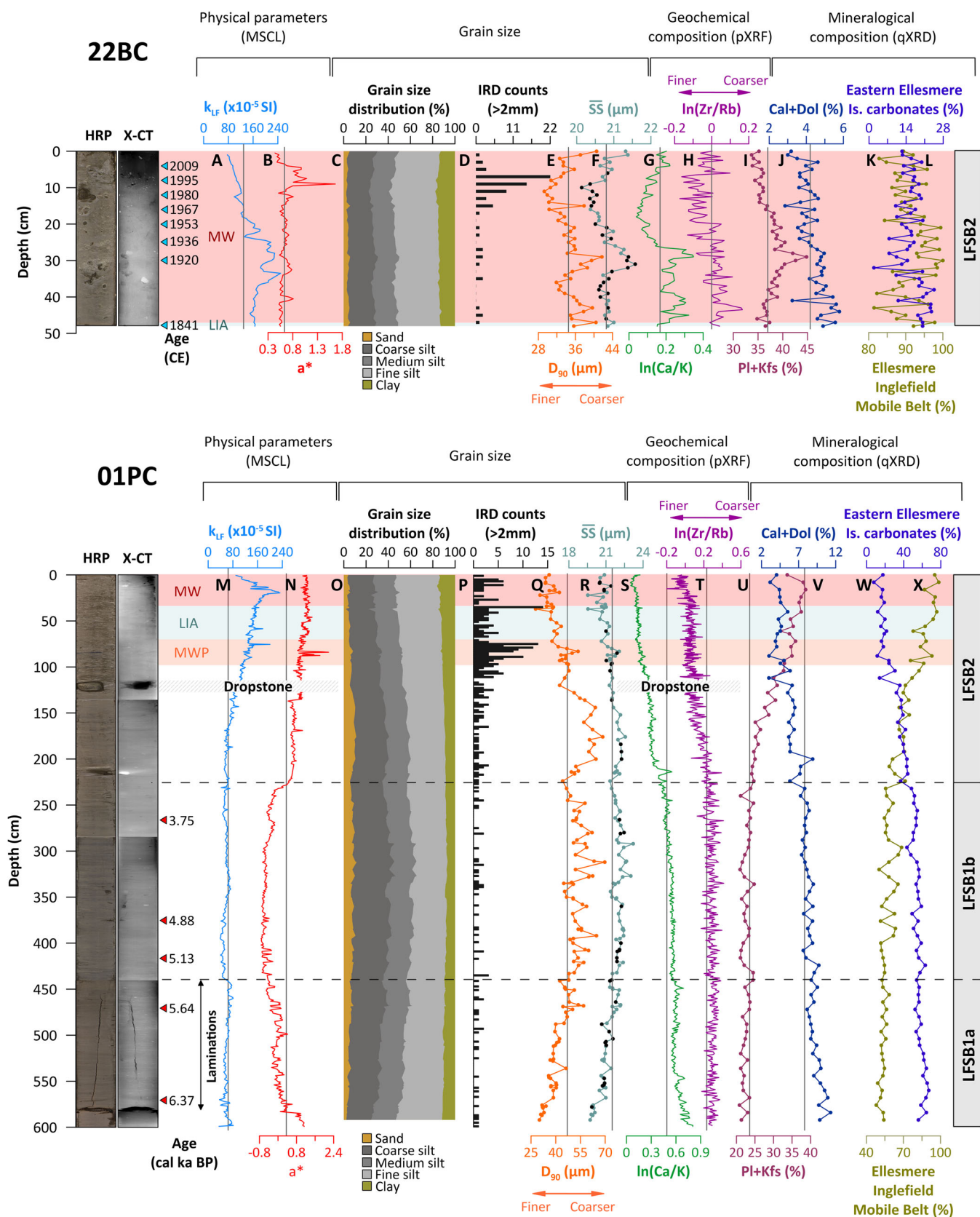


Figure 4. High-resolution core photography, X-CT image, magnetic susceptibility (k_{LF}), a^* , grain size distribution, IRD counts (> 2 mm fraction), D_{90} (μ m), mean size of sortable silt fraction (\overline{SS}), chemical and mineralogical tracers, SedUnMix results with the proportions of sediment from Eastern Ellesmere Island carbonates (blue) and Ellesmere-Ingfield Mobile Belt (gray), and sedimentary units of cores 22BC and 01PC. The vertical lines represent the median of the data for each proxy. Red triangles represent levels of radiocarbon ages; blue triangles represent the levels of ^{210}Pb dates. The black dots on the \overline{SS} curve represent samples that do not pass the reliability test of a downcore correlation coefficient >0.5 between \overline{SS} and $SS\%$. [Color figure can be viewed at [wileyonlinelibrary.com](https://onlinelibrary.wiley.com/doi/10.1002/jqs.70005)]

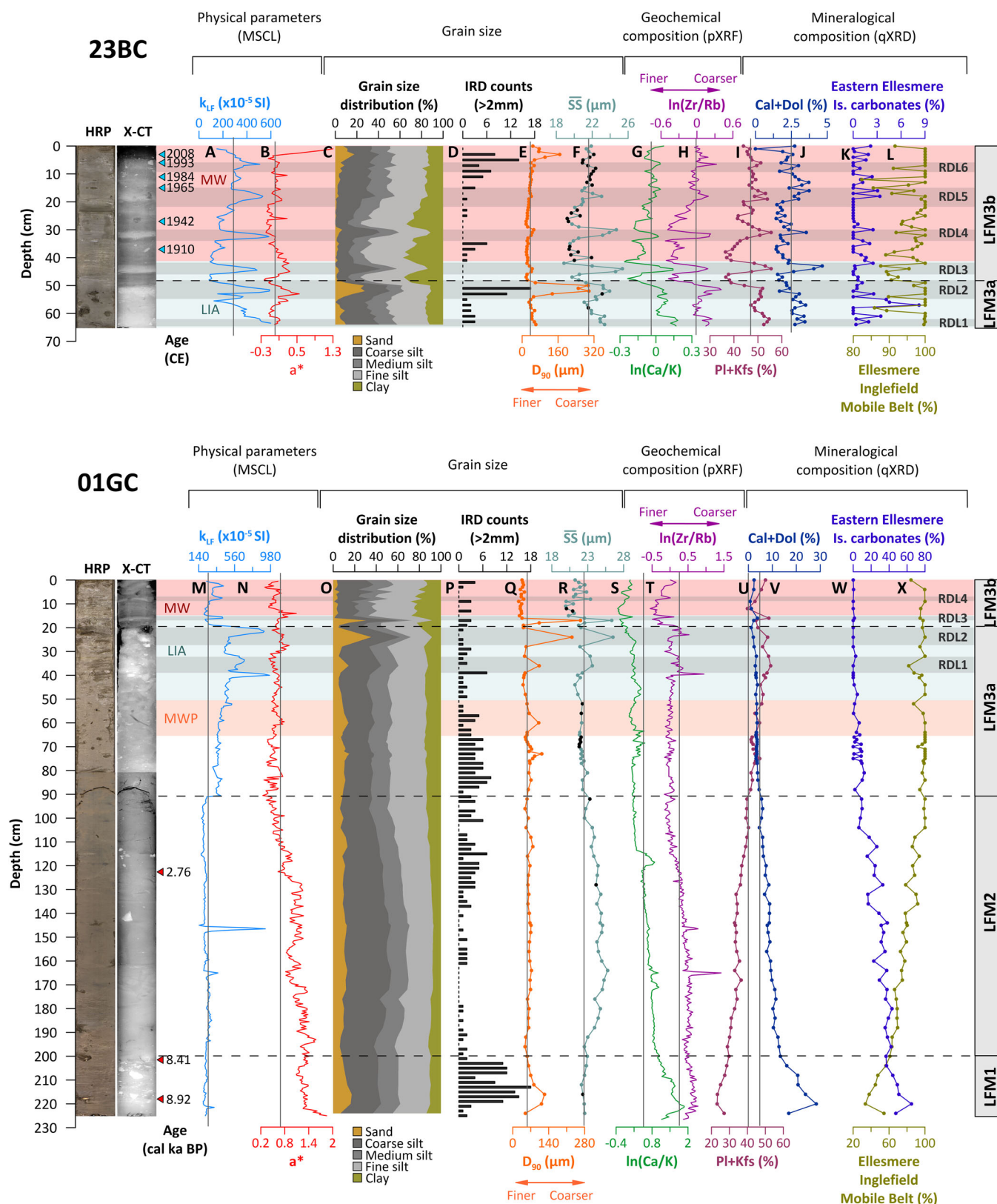


Figure 5. High-resolution core photography, X-CT image, magnetic susceptibility (k_f), a^* , grain size composition, IRD counts (>2 mm fraction), D_{90} (μm), mean size of sortable silt fraction (SS), chemical and mineralogical tracers, SedUnMix results with the proportions of sediment from Eastern Ellesmere Island carbonates (blue) and Ellesmere–Inglefield Mobile Belt (gray), and sedimentary units of cores 23BC and 01GC. The vertical lines represent the median of the data for each proxy. Red triangles represent levels of radiocarbon dates; blue triangles represent the levels of ^{210}Pb dates. Rapid deposited layers (RDLs) are numbered and highlighted in gray boxes. The black dots on the SS curve represent samples that do not pass the reliability test of a downcore correlation coefficient >0.5 between SS and SS%. [Color figure can be viewed at [wileyonlinelibrary.com](https://onlinelibrary.wiley.com/doi/10.1002/jqs.70005)]

carbonate content of all the cores studied (up to 30%). The mineralogical assemblage indicates that the main sediment source up to ~220 cm comes from the Eastern Ellesmere Island carbonates (~50%–65%), before shifting to the

Ellesmere–Inglefield Mobile Belt source (~40%–60%) (Fig. 5). The transition from LFM1 to LFM2 is smooth with a progressive decrease in the D_{90} , grain size, and the detrital carbonate content. LFM1 is interpreted as a mix of sediments deposited

close to the grounded ice position of Mittie Glacier and ice-rafted material deposited by icebergs and sea ice coming from outside Smith Bay.

LFM2 (200–91 cm; 8.4 to 1.8 cal ka BP) is a coarse-grain mud slightly bioturbated according to X-CT scans (Fig. 5). The physical properties are characterized by a high but constant k_{LF} and a gradual decrease in a^* . Initiated in LFM1, the decrease in $\ln(\text{Ca}/\text{K})$ and $\text{Cal}+\text{Dol}$ continues, but the mineralogical assemblage becomes enriched in $\text{Pl}+\text{Kfs}$. The sediments are mainly composed of a mix of sand, coarse, and medium silts. ΣS values increase and reach high values ($\sim 24 \mu\text{m}$) in LFM2, suggesting the presence of strong near-bottom currents at that time. The IRD count shows an increase of millimeter–centimeter clasts toward the top of the lithofacies with a centimeter-sized rock around 138–144 cm and some rock fragments around 112–120 cm (Fig. 5). LFM2 could be

deposited by a continuous supply of rather coarse particles by meltwater plumes from the grounding line during IIS retreat.

LFM3 (core 01GC: 91–0 cm, core 23BC: 65–0 cm; 1.8 cal ka BP to present day) is divided into two sub-lithofacies. LFM3a is composed of grayish brown (2.5YR 5/2) to light brownish gray (2.5Y 6/2) silty to sandy mud with bioturbation and disseminated gravel-sized clasts. The transition between LFM3a and LFM3b is made by a change in sediment color and granulometry. LFM3b is mainly composed of grayish brown (10YR 5/2) clayey silts with light brownish gray (2.5Y 6/2) silty to sandy centimeter-scale laminations with a high proportion of medium- to coarse-grained sediments ($D_{90} = 41\text{--}297 \mu\text{m}$; Fig. 5) and disseminated gravel-sized clasts interpreted as IRD. This facies is characterized by the occurrence of six rapidly deposited layers (RDLs; Figs. 5 and 6): RDL6 (6–8 cm), RDL5 (15–22 cm), RDL4 (30–34 cm), RDL3 (42–46 cm), RDL2 (48–56 cm) and RDL1 (62–72 cm). Their

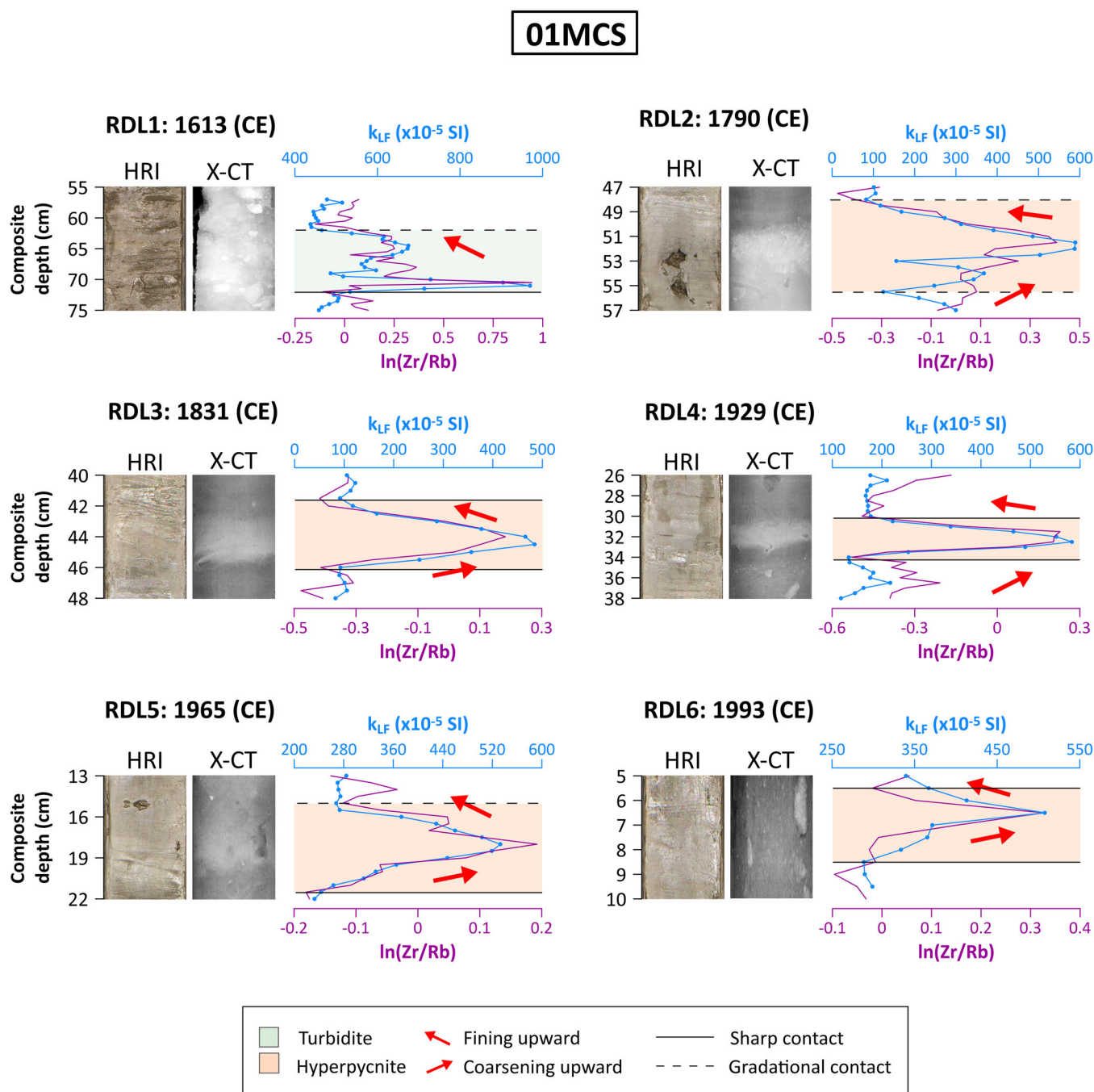


Figure 6. X-CT scan image, high-resolution core photography, $\ln(\text{Zr}/\text{Rb})$ ratio and k_{LF} for the RDLs identified in cores 23BC and 01GC. RDL6 to RDL2 depths are from core 22BC, and RDL1 depth is from the composite core 01MCS. [Color figure can be viewed at wileyonlinelibrary.com]

identification was established by a sharp increase in the physical, geochemical, and mineralogical parameters along with the grain size (D_{90} and \overline{SS}) data. RDL1 displays a normal grading sequence, while RDL2 to RDL6 display a laminated inverse grading sequence. X-CT scan images and the number of >2 mm clasts show that gravel-sized clasts are more frequent between 54–50 cm, 38–34 cm, and 12–2 cm (Fig. 5). Generally decreasing, the \overline{SS} values display punctual, short, and rapid increases concomitant with the deposition of the RDLs, suggesting the deposition of the RDL is linked to the occurrence of short events of strong near-bottom currents. LFM3 was likely deposited during a period of higher input of glacial meltwater outwash.

Chronology

The ^{210}Pb activity profiles of cores 22BC and 23BC (Fig. S5) show an exponential decay for both cores with ^{210}Pb supported values of 32.3 and 33.6 Bq kg^{-1} , respectively. These ^{210}Pb supported values are consistent with those observed in the Smith Sound region that range between ~20–30 Bq kg^{-1} (e.g., Bailey et al., 2013; Ribeiro et al., 2021).

The age model for the composite core 01SBCS indicates that sediments span the last 6.6 cal ka BP, with a median calculated sedimentation rate of ~100 cm ka^{-1} (Figs. 8(A) and S5(A)). This model reveals three major changes in sedimentation rates throughout the Holocene: a high sedimentation rate of 141–97 cm ka^{-1} during the Middle Holocene (6.6 to 3.8 cal ka BP; 612–281 cm depth), a decline followed by a stagnation of 64 cm ka^{-1} during the Middle to Late Holocene (3.8 cal ka BP to 1829 CE; 280–50.5 cm depth), and a very high sedimentation rate of 214–321 cm ka^{-1} during the last 190 years (50.5–0 cm depth). The age model of the composite core 01MCS is constrained by the presence of RDLs (Fig. 6). As these are instantaneous deposits, the six RDLs were excluded from the age-model, resulting in an event-free sedimentary record (Figs. 8(B) and S5(B)). Additionally, a surface mixed layer (SML) is present in core 23BC (~0–2 cm). Data from this zone were not used to establish the chronology based on excess ^{210}Pb (Fig. S5(B)). Thus, 01MCS spans the last 9.2 cal ka BP with a median calculated sedimentation rate of ~30 cm ka^{-1} (Fig. 8(B) and S5(B)). This model reveals four major changes in sedimentation rates throughout the Holocene: a low sedimentation rate of 23–33 cm ka^{-1} during the Early Holocene (9.2 to 8.4 cal ka BP; 257–231.5 cm depth), a decline to 14 cm ka^{-1} during the Middle Holocene (8.4 to 2.9 cal ka BP; 231–156.5 cm depth), an increase to 25–41 cm ka^{-1} during the Middle to Late Holocene (2.9 cal ka BP to 1900 CE; 156.5–40 cm depth), and a high sedimentation rate of 163–223 cm ka^{-1} during the last 120 years (40–0 cm depth). We acknowledge that the high sedimentation rates observed in 01SBCS and 01MCS cores during the last 190 and 120 years, respectively, might be caused by an absence of ^{14}C dates at the transition from the ^{210}Pb - and ^{14}C -dated intervals (Fig. 8). However, we do not consider this a significant source of bias, as similarly high sedimentation rates (~0.4–0.7 cm year^{-1}) have been reported in sediment cores from southern Nares Strait, as documented by Jackson et al. (2021) and Ribeiro et al. (2021).

Discussion

Early Holocene depositional processes (9.2 to 8.2 cal ka BP)

Following the last deglaciation, the beginning of the Holocene was a time of rapid climate and environmental change. The orbitally driven high boreal summer insolation (Fig. 9(A)), which peaked around 11 cal ka BP, resulted in the final collapse of the IIS and GrIS, as well as their landward retreat in

northeastern Baffin Bay (e.g., Dyke et al., 2002; Kaufman et al., 2004; Laskar et al., 2004; England et al., 2006; Marcott et al., 2013; Jennings et al., 2014, 2017; Lecavalier et al., 2017; Buizert et al., 2018; Dalton et al., 2020). Based on the dating of two *Macoma calcaria* shells in this study, the Early Holocene sequence was only recognized in the ice-proximal setting cores (Fig. 5). LFM1 is characterized by high wet bulk density (up to 2 g cm^{-3}) and a low sedimentation rate (~23–33 cm ka^{-1}), apparently recurrent in the NW Baffin Bay region (Pieńkowski et al., 2012, 2013; Jennings et al., 2019; Jackson et al., 2021; Stevenard et al., 2022; Okuma et al., 2023). The mineralogical assemblages are not uniform throughout the unit and appear similar to those described by Caron et al. (2020) in a core from Kane Basin (AMD14-Kane2B). At the base of the unit, between 9.2 and 8.6 cal ka BP, rather high concentrations of detrital carbonates (~33%) indicate sediments from a nonlocal source (Figs. 1 and 9). According to the SedUnMix model, 65% of these sediments were derived from an eastern Ellesmere Island carbonate source (Fig. 5). The LFM1 diamict suggests that sedimentary dynamics near core 01GC were mainly controlled by ice-rafted material deposited by icebergs and sea ice coming from outside Smith Bay (Fig. 10(A)). We estimate, based on the ice reconstructions of Dalton et al. (2020), that these sediments were likely deposited during both the westward sea-ice retreat in Makinson Inlet (England et al., 2006) and the early stage of deglaciation of Nares Strait (Jennings et al., 2011, 2019; Georgiadis et al., 2018; Caron et al., 2019, 2020; Stevenard et al., 2022).

Around 8.6 to 8.2 cal ka BP, a pronounced shift in the mineralogical assemblage and the grain size is observed (Fig. 5). A long-term decrease in detrital carbonates, IRD input, and a change to finer-grain-size sediment (mainly silt) suggest a progressive reduction in the carbonate-rich iceberg transport into Smith Bay (Figs. 5 and 9). The \overline{SS} records indicate enhanced near-bottom current velocity from ~8.4 cal ka BP (Fig. 9(D)). Consequently, the observed shift in sediment provenance, the low sedimentation rates (14–33 cm ka^{-1}) and the increase in the near-bottom current velocity recorded in LFM1 are consistent with the final stage of deglaciation in Nares Strait between 8.5 and 8.2 cal ka BP and the establishment of an open marine connection between the Arctic Ocean and Baffin Bay (e.g., Dyke et al., 2002; Knudsen et al., 2008; Jennings et al., 2011, 2019, 2022; St-Onge and St-Onge, 2014; Georgiadis et al., 2018; Caron et al., 2019, 2020; Kelleher et al., 2022). The mineral assemblage also displayed rather high concentrations in $\text{Pl}+\text{Kfs}$ (~30%), masked by the significant carbonate input until 8.6 cal ka BP (Figs. 5 and 9(C)). This suggests a continuous input of sediments from a local source derived from the Ellesmere Inglefield Mobile Belt (~50%). At that time, the presence of a diamict and shallow water depths (~207 m depth; Fig. 2) likely indicates that Mittie Glacier remained grounded and extended further into a largely unglaciated Smith Bay (Dalton et al., 2020), close to the position of sediment core 01GC (Fig. 10(A)). When Mittie Glacier retreated during the deglaciation, the unsorted sediment assemblage was deposited close to its grounding line position and mixed with the carbonate-rich IRD originating from Nares Strait and Makinson Inlet.

Middle to Late Holocene depositional processes (8.2 to 3 cal ka BP)

Higher boreal summer insolation during the Early to the beginning of the Middle Holocene led to a period of summer temperatures warmer than present conditions throughout the Arctic (Fig. 9(A)), known as the Holocene Thermal Maximum

(HTM) with a boreal summer insolation maximum around 8 cal ka BP (Kaufman et al., 2004; Mayewski et al., 2004; Wanner et al., 2008; Renssen et al., 2012; Marcott et al., 2013; Briner et al., 2016; Lecavalier et al., 2017; Bader et al., 2020). This period in Makinson Inlet was characterized by a relative sea level 10 to 40 m higher than the present day (Blake, 1993). In both the distal and proximal environments, the \overline{SS} records indicate enhanced near-bottom current velocity during the Middle to Late Holocene (~7–5 cal ka BP), which decreased progressively during the Late Holocene, in line with further decreasing boreal summer insolation (Fig. 9(A),(D)). These results are consistent with findings from cores in Cape Norton Shaw Inlet (Stevenard et al., 2022) and Smith Sound (core 2001LSSL-014PC; McCave and Andrews, 2019b), and they reinforce the interpretation that the Middle to Late Holocene in this region was characterized by a gradual weakening of

circulation associated with declining insolation and reduced meltwater input (McCave and Andrews 2019b).

In the ice-proximal setting, the detrital carbonates content in LFM2 continues to decrease after the end of the Early Holocene, suggesting a reduced input of carbonate-rich sediments from Nares Strait and Makinson Inlet into the bay via ice rafting transport (Fig. 5). This decline coincides with a progressive weakening of near-bottom current velocities, as indicated by the \overline{SS} record. The associated reduction in hydrodynamic energy likely limited the lateral transport and redistribution of ice-rafted debris within Smith Bay, further supporting the interpretation of diminished circulation during the Middle to Late Holocene. In contrast, in the ice-distal setting, the mineralogical assemblage, which is a mixture of Ellesmere Inglefield Mobile Belt and Eastern Ellesmere Island Carbonates sources, remains relatively constant (Fig. 4). Given

	Cores	Units	X-CT	HRI	Lithofacies	Colour	Sedimentary structures	D ₉₀ (µm)	Depositional processes
ICE DISTAL	22BC	LFB2	20 cm	20 cm	Silty mud with few IRDs	2.5Y 4/3 Olive brown	Slightly bioturbated massive mud	35	•Ice rafting •Meltwater plumes
			40 cm	40 cm					
	01PC	LFSB2	190 cm	190 cm	Silty mud with few IRDs	2.5Y 4/3 Olive brown	Massive mud	46	Meltwater plumes
			210 cm	210 cm					
		LFSB1b	330 cm	330 cm	Silty mud	2.5Y 4/3 Olive brown	•Slightly bioturbated massive mud •Pyritized microfaunal burrows	54	Meltwater plumes
ICE PROXIMAL			350 cm	350 cm					
		LFSB1a	520 cm	520 cm	Silty laminated mud	2.5Y 4/2 Dark grayish brown	•Bioturbated laminated mud •Pyritized microfaunal burrows	41	Meltwater plumes
			575 cm	575 cm					
	23BC	LFM3	30 cm	30 cm	Silty mud with succession of hyperpycnites deposits	2.5Y 5/2 Grayish brown 2.5Y 6/2 Light brownish gray	•Slightly bioturbated mud •RDLs •IRDs	52	•Ice rafting •Meltwater plumes •Hyperpycnal flow
			50 cm	50 cm					
	01GC	LFM3b	5 cm	5 cm	Silty mud with succession of hyperpycnites deposits	2.5Y 5/2 Grayish brown 2.5Y 6/2 Light brownish gray	•Slight coring disturbance bending •RDLs •IRDs	50	•Ice rafting •Meltwater plumes •Hyperpycnal flow
			18 cm	18 cm					
		LFM3a	30 cm	30 cm	Clay to silt layer containing very coarse sand with small clasts	2.5Y 5/2 Grayish brown	Lithified mud (small clasts)	69	•Ice rafting •Meltwater plumes
			50 cm	50 cm					
		LFM2	150 cm	150 cm	Homogeneous silty mud	2.5Y 4/3 Olive brown	Slightly bioturbated mud	63	Meltwater plumes
			170 cm	170 cm					
		LFM1	200 cm	200 cm	Clay to silt mud containing coarse sand with clasts	2.5Y 4/3 Olive brown	•Massive lithified mud with intact shells •IRDs	79	•Ice rafting •Meltwater plumes
			220 cm	220 cm					

Figure 7. Summary of the physical characteristics, average grain size data (D₉₀), and interpretation of the depositional processes of the lithofacies identified in cores 22BC, 01PC, 23BC, and 01GC. [Color figure can be viewed at [wileyonlinelibrary.com](https://onlinelibrary.wiley.com/doi/10.1002/jqs.70005)]

that core 01PC is located at the junction between Smith Bay and Makinson Inlet waters, and considering the decrease in carbonate supply from Nares Strait after its opening, we estimate that the constant supply of detrital carbonates likely originates from Makinson Inlet.

From 6.6 cal ka BP, the comparison between LFM2 and LFSB1 indicates similar variations. The low sedimentation rate recorded in LFM2, coupled with a decrease in the sedimentation rate of LFSB1, coincides with a slight increase in coarse-grained sediments and the PI+Kfs content in both the glacier proximal environment and in Smith Bay (Figs. 4 and 5). The decrease in the sedimentation rates and the increase in coarse-grained sediments may indicate a decline in the input of sea-ice rafted fine-grained sediments, which were replaced by an enhanced delivery of suspended sediments in the form of glacial flour silt (Fig. 10(B)), suggesting a landward retreat of Mittie Glacier and the surrounding glaciers. LFSB1a records several light-colored centimeter-scale laminations that are absent in LFM2 (Fig. 4), suggesting a period between 6.4 and 5.4 cal ka BP influenced by meltwater outwash dominated by suspension setting in an ice distal environment. Both LFM2 and LFSB1b are clast-poor with traces of bioturbation, suggesting deposition under more productive surface waters (Figs. 7 and 9(E)), indicative of less extensive surface ice cover in Smith Bay after 5.4 cal ka BP. This interpretation is supported by biomarker-derived estimates of sea-ice extent from sediment cores in southern Nares Strait, which suggest reduced sea-ice cover and duration

compared to the present around 6 cal ka BP (Fig. 9(B); Georgiadis et al., 2018; Jackson et al., 2021). In this context, we assume that Mittie Glacier and the glaciers surrounding Smith Bay were retreating or had already become land-based in response to the warm conditions during the Middle Holocene. It is likely that Smith Bay was largely sea ice free during summer after 5.4 cal ka BP (Fig. 10(B)).

Late Holocene to modern depositional processes (3 cal ka BP to present day)

Following the deglaciation of Smith Bay, the upper part of LFM2 and LFSB2, characterized by an increase in IRD content and finer-grained sediments (Fig. 9(E)), suggests an intensification of glacial erosional processes in Smith Bay at that time. Regarding the period between 3 and 2 cal ka BP, the increase in IRD likely represents the establishment of cooler conditions, linked to the first pulse of the Neoglacial and the early stage of the regrowth of the tidewater glaciers surrounding Smith Bay (Briner et al., 2009, 2016; Solomina et al., 2015; McKay et al., 2018).

From ~2 cal ka BP, the increase in k_{LF} observed in LFM3a and LFSB2 (Figs. 4 and 5), along with a net augmentation in the PI+Kfs percentage and a decrease in $\ln(\text{Ca/K})$, associated with finer-grained sediments (i.e., fine silts and clays; ~50%), is interpreted as an intensification of glacial erosional processes and calving activity during the second major Neoglacial pulse (McKay et al., 2018). In the cores close to Mittie Glacier, the IRD abundance is lower than in the cores in Smith Bay

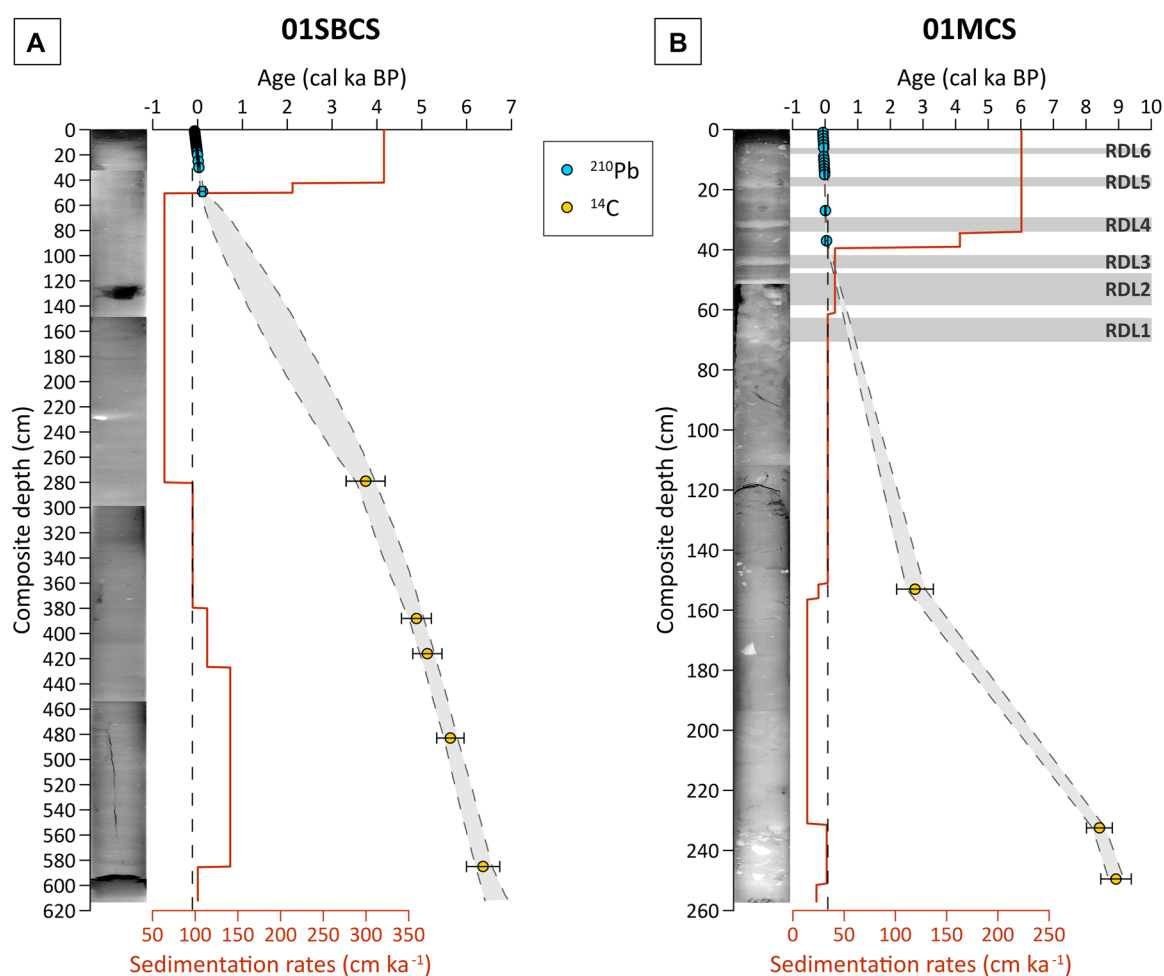


Figure 8. Composite age–depth model for cores (A) 01SBCS and (B) 01MCS constructed using ^{210}Pb and ^{14}C ages. The Bayesian age–depth model was constructed using the R package rbacon (version 3.3.1; Blaauw and Christen, 2011). The gray shading represents the chronological uncertainties (95% confidence interval). The black dotted line represents the median of the data for the sedimentation rates. The estimated sedimentation rates in cm ka^{-1} are also shown. [Color figure can be viewed at [wileyonlinelibrary.com](https://onlinelibrary.wiley.com/terms-and-conditions)]

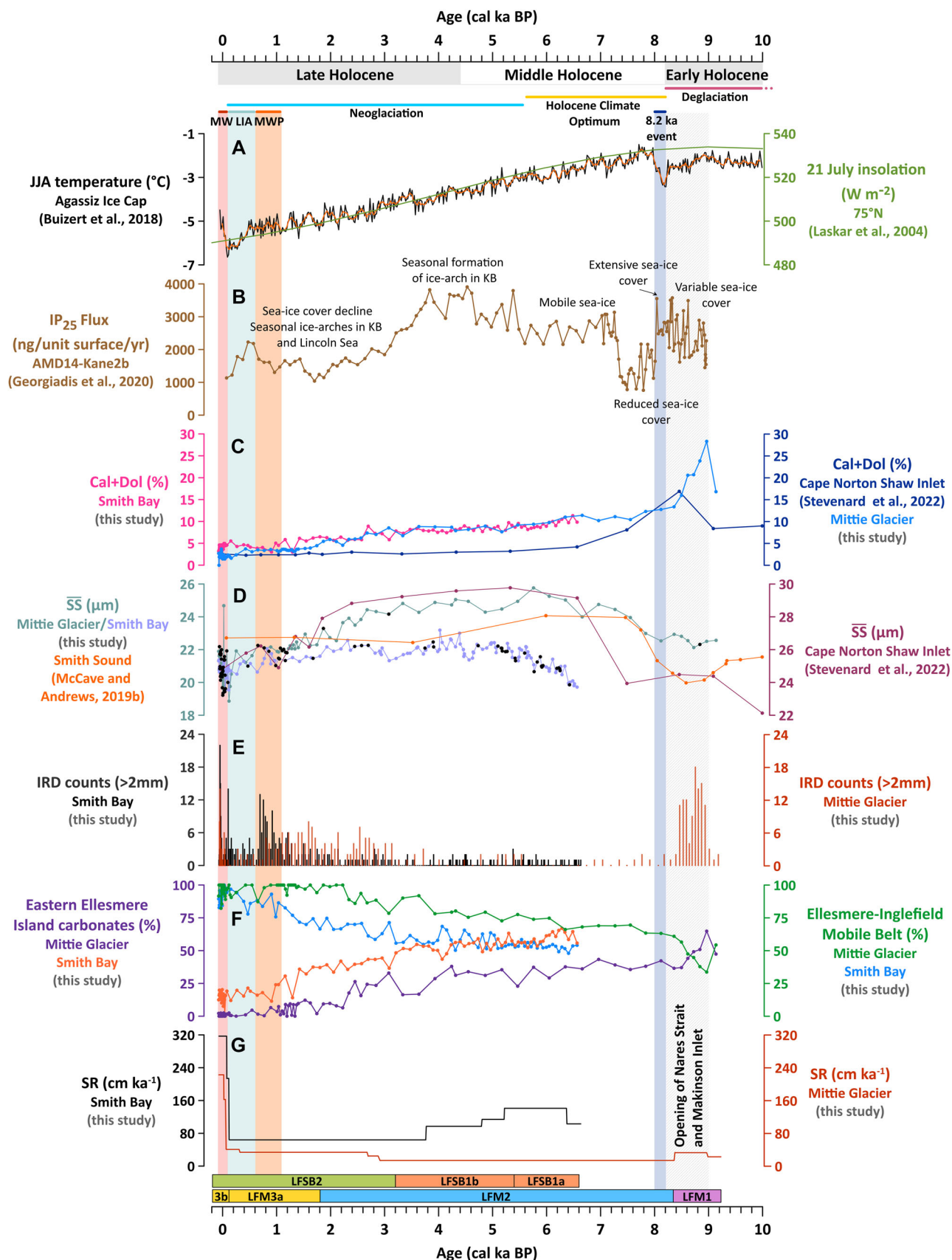


Figure 9. Comparison of proxies used in this study (01SBCS: Smith Bay, 01MCS: Mittie Glacier) with paleoenvironmental proxies. (A) Reconstructed summer temperature (°C) of the Agassiz Ice Cap (Buizert et al., 2018) and 21 July insolation at 75° N (Laskar et al., 2004); (B) Proxy charting sea-ice conditions (lipid biomarker—IP₂₅) from AMD14-Kane2b (Georgiadis et al., 2018); (C) Cal+Dol from cores 01SBCS (pink, this study), 01MCS (light blue, this study) and AMD1803-01PC (dark blue, Stevenard et al., 2022); (D) Mean size of sortable silt fraction (SS) from cores 01SBCS (light purple, this study), 01MCS (teal, this study), AMD1803-01PC (crimson, Stevenard et al., 2022) and 2001LSSL-014PC (orange, McCave and Andrews, 2019b); (E) IRD count (>2 mm) of cores 01SBCS (black, this study) and 01MCS (red, this study); (F) Mineralogical sources (%) from Eastern Ellesmere Island (pink and orange, this study) and from the Ellesmere-Inglefield Mobile Belt (green and blue, this study); (G) Sedimentation rates (cm ka⁻¹) for cores 01SBCS (black, this study) and 01MCS (red, this study). The black dots on the SS curves represent samples that do not pass the reliability test of a downcore correlation coefficient >0.5 between SS and SS%. Note that the age-depth data from Stevenard et al. (2022) were recalculated with a $\Delta R = 71 \pm 69$ years BP. [Color figure can be viewed at [wileyonlinelibrary.com](https://onlinelibrary.wiley.com/doi/10.1002/jqs.70005)]

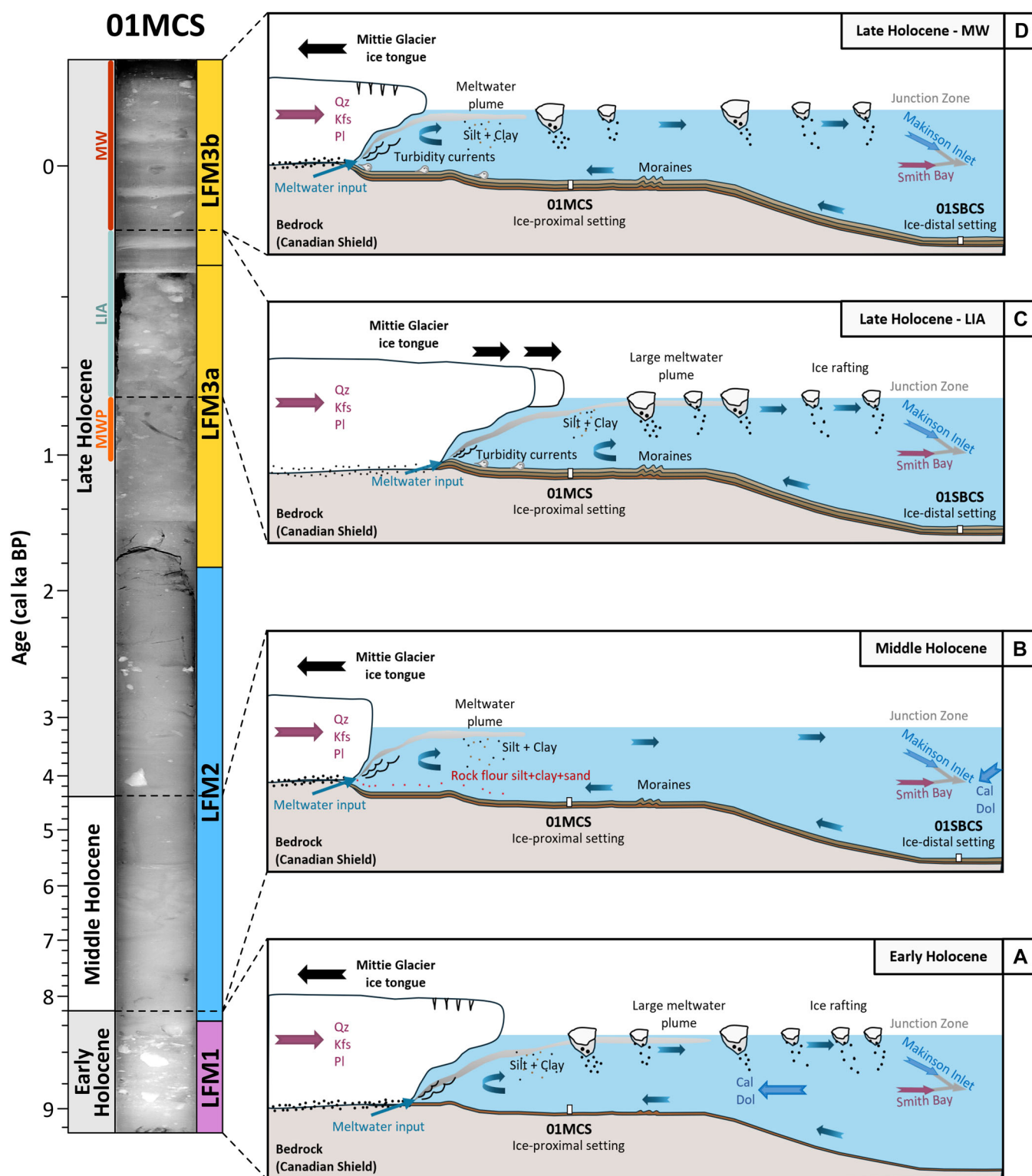


Figure 10. Correlation of X-CT scans, composite core 01MCS lithofacies, and the reconstruction of Mittie Glacier sedimentary processes and environmental conditions in Smith Bay during (A) the Early Holocene (9.2 to 8.2 cal ka BP), (B) the Middle Holocene (8.2 to 3 cal ka BP), and the Late Holocene (3 cal ka BP to present), with a distinction between (C) the Little Ice Age (LIA) and (D) the Modern Warming (MW). [Color figure can be viewed at [wileyonlinelibrary.com](https://onlinelibrary.wiley.com/doi/10.1002/jqs.70005)]

(Fig. 9(E)), suggesting that Mittie Glacier was probably advanced in the bay with a floating tongue or ice shelf extending close to the proximal cores location (Fig. 10(C)), and had probably reached its Holocene maximum extension during the Little Ice Age (LIA; ~1350–1850 CE; Grove, 1988; Jones and Mann, 2004; Miller et al., 2012). Our results align with those recorded in cores AMD1803-02BC and -01PC from Cape Norton Shaw Inlet (Stevenard et al., 2022) and confirm the establishment of colder conditions associated with glacier growth in the area during that time (Fig. 9).

The LIA interval is also marked by the deposition of three thin RDLs (~4–6 cm) only recorded in the ice-proximal setting (Fig. 6). These three RDLs (RDL1, RDL2, RDL3), rich in PI and Kfs, are characterized by abrupt changes in all detrital proxies (Figs. 5 and 6). The k_{LF} and $\ln(Zr/Rb)$ profiles of RDL1 display a normal grading sequence, which is typical of classical turbidites, while RDL2 to RDL6 display a laminated inverse grading sequence, which is interpreted as hyperpycnites deposited from hyperpycnal turbidity currents (Fig. 6; Bouma, 1962; Mulder et al., 2003; Rodríguez-Cuicas et al., 2023). In the ice-proximal environment,

turbidites can be linked to snowmelt runoff and meltwater plumes (Dowdeswell et al., 2015), while hyperpynites are believed to form in the marine environment when river discharge enters the ocean with suspended concentrations in excess of 36 kg m^{-3} (e.g., Mulder et al., 2003; Zavala, 2020). These RDLs show an increase in both $\text{Pl}+\text{Kfs}$ and $\text{Cal}+\text{Dol}$ suggesting that sedimentary inputs are driven by a mix of sources. Thus, most of the sediments are believed to originate from Mittie Glacier (86%–94%), while the secondary detrital source (rich in detrital carbonate) is likely brought from the western side of Makinson Inlet via large subglacial lake discharges and subglacial hydrological networks (Fig. 2(A); Gray et al., 2024).

Since around 1900 CE, a higher sedimentation rate ($163\text{--}223 \text{ cm ka}^{-1}$), along with an increase in the content of coarse-grained sediments, suggests increased runoff from snowmelt and meltwater plumes. High sedimentation rates ($\sim 400\text{--}700 \text{ cm ka}^{-1}$) are also recorded in sediment cores from southern Nares Strait and interpreted as reflecting a period of shorter ice-arch durations or failure in Kane Basin (Jackson et al., 2021; Ribeiro et al., 2021). High sedimentation rates indicate the occurrence of a much warmer period associated with glacier retreat during modern warming (Figs. 9(E) and 10(D); MW). The sudden increase followed by a decrease in the \overline{SS} values at this time is likely driven by changes in hyperpynal flow velocity associated with the RDLs and increased runoff from snowmelt and meltwater plumes (Fig. 9(E)). During the MW, three hyperpynites: RDL4,

RDL5, and RDL6 were deposited between 1929 and 1993 CE (Fig. 6). Recently, Gray et al. (2024) showed that a subglacial lake was draining and refilling in cycles of ~ 14 years since at least 1993 upstream of the western arm of Mittie Glacier (Fig. 2(A)). Our results suggest that this subglacial lake could be the origin of the hyperpynal deposits, as it was likely already formed during the LIA and could have drained and refilled over longer periods. Based on our age-depth models, we estimate a 41-year cycle for RDL2 and RDL3, and a 36-year cycle for RDL4 and RDL5. The most recent RDL6 is dated at 1993 CE, which is the same age determined by Gray et al. (2024; Fig. 6). An increase in total precipitation and warmer summers recorded in 1991 at the Grise Fiord meteorological station seems to have played a significant role in refilling the subglacial lake, leading to its discharge in 1993 (Fig. 11(A),(B)). Thus, the climate seems to trigger the refill/drainage of the subglacial lake and to influence the duration of the cycles, with longer cycles under colder conditions (LIA) and shorter cycles under warmer conditions (MW).

Between ~ 1993 and 2008 CE, we observed an IRD-rich layer associated with coarse-grained sediments in core 23BC (Fig. 11(B)–(D)), but without an increase in other detrital proxies, as was the case with the RDLs. The dating of this layer correlates well with the 1992–2007 period, during which the last surge of Mittie Glacier was identified in both satellite imagery and velocity data from the eastern arm of the glacier (Copland et al., 2003, 2024; Short and Gray, 2005; Sharp et al., 2014;

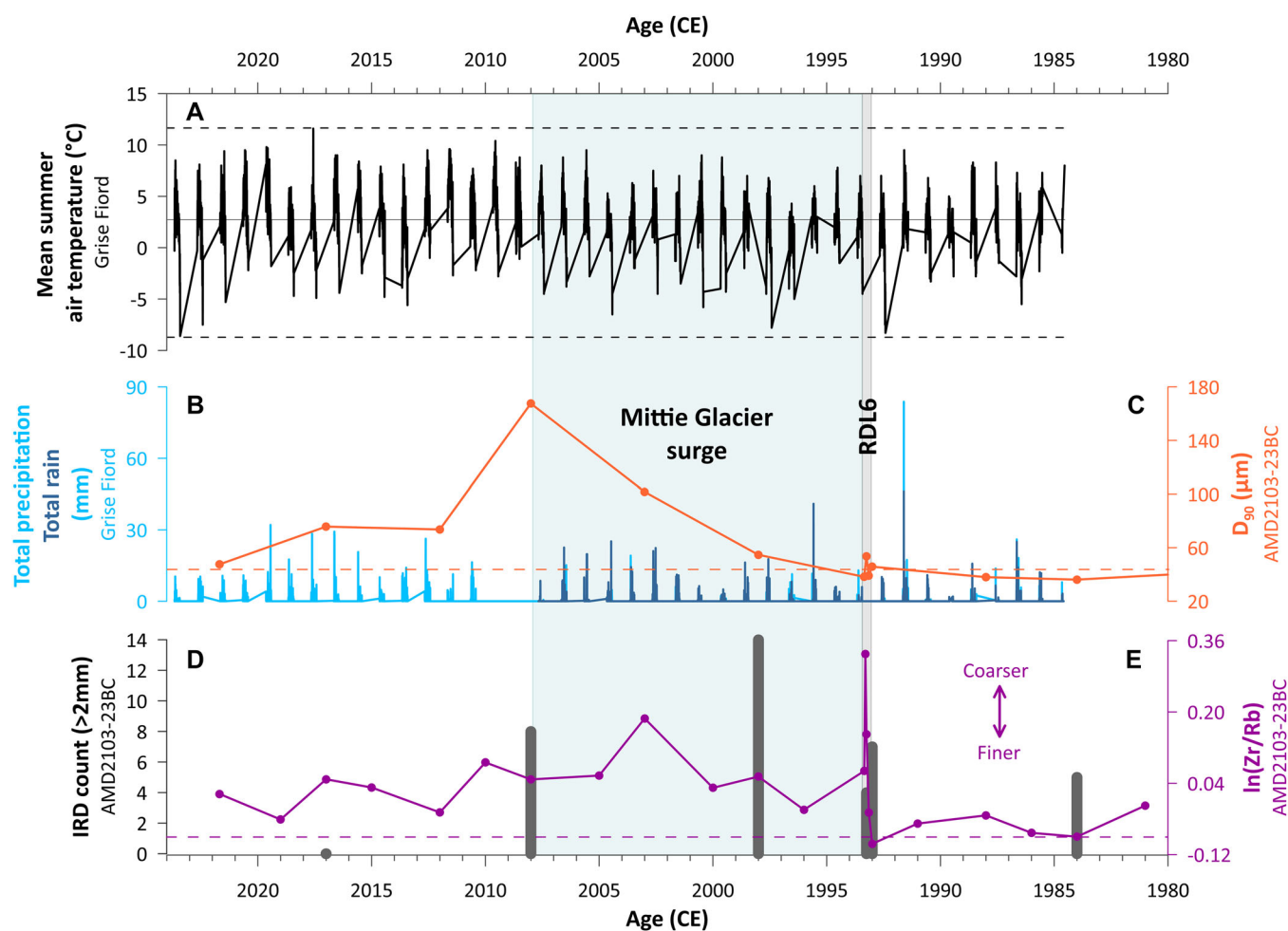


Figure 11. Comparison of (A) historical summer mean air temperature data at Grise Fiord (black, source: <https://climate.weather.gc.ca>), (B) total precipitation (light blue) and rain (navy blue) data at Grise Fiord (source: <https://climate.weather.gc.ca>), (C) D_{90} (μm), (D) IRD count ($>2\text{mm}$), and (E) $\ln(\text{Zr}/\text{Rb})$ profiles from core 23BC. The dashed lines represent the maximum and minimum values for temperature, horizontal lines indicate the median for each proxy, the gray box highlights RDL6, and the blue box represents the last surge of Mittie Glacier (1992–2007 CE; Copland et al., 2003, 2024). [Color figure can be viewed at [wileyonlinelibrary.com](https://onlinelibrary.wiley.com/terms-and-conditions)]

Van Wychen et al., 2016, 2020). In cores 23BC, the highest number of IRD is recorded ~1998 CE (Fig. 11(D)), which correlates well with the 1994–1999 period during which the glacier advanced >7 km. Therefore, we suggest that the coarse layer observed at the top of core 23BC was likely deposited during the last surge of Mittie Glacier, which was induced by the dynamics of the eastern arm of the glacier. The increase in total precipitation and warmer summers recorded in 1991 at the Grise Fiord meteorological station could have destabilized the glacier by water infiltration at the bedrock-glacier interface and triggered the surge, together with flotation of the glacier terminus due to long-term thinning (Copland et al., 2024).

Conclusion

Based on a multiproxy approach applied to sediment cores collected in the outer part of Smith Bay (22BC and 01PC) and near the terminus of Mittie Glacier (23BC and 01GC), we provide a detailed reconstruction of the sedimentary dynamics in the northeastern part of Manson Icefield over the last 9.2 cal ka BP. We used physical, mineralogical, and geochemical properties, as well as grain size distribution, to document the composition, provenance, and transportation processes of the detrital sediments. The findings of this study lead to the following key conclusions:

- Physical, mineralogical, and geochemical properties associated with a low sedimentation rate ($\sim 30 \text{ cm ka}^{-1}$) and enhanced near-bottom current velocity in sediment core 01GC support the hypothesis of the gradual opening of Nares Strait between 8.8 and 8.2 cal ka BP.
- After 8.2 cal ka BP, sediment provenance is primarily dominated by an Ellesmere Inglefield Mobile Belt source, rich in Pl and Kfs, suggesting a sedimentation predominantly influenced by sediment discharge from Mittie Glacier and the glaciers surrounding Smith Bay.
- Lower sedimentation rates ($< 14 \text{ cm ka}^{-1}$) recorded between 8.4–2.9 cal ka BP, along with the coarse-grained sediments in LFM2 and LFSB1, indicate a landward retreat of Mittie Glacier and sea-ice-free conditions during summer in Smith Bay starting around 5.4 cal ka BP. The \overline{SS} records reveal intensified near-bottom currents in Smith Bay at the beginning of the Middle Holocene, followed by a gradual weakening linked to declining insolation and meltwater input into the bay.
- During the Neoglacial period, the increase in IRD content and finer-grained sediments in ice-proximal sediment cores suggests an advance of Mittie Glacier into Smith Bay, with an ice shelf or glacier ice tongue extending close to the location of the ice-proximal cores, where it probably reached its Holocene maximum extent.
- Climate probably triggers and influences the duration of discharge of a subglacial lake upstream of the western arm of Mittie Glacier, causing hyperpycnal events since the LIA. The events follow a 41-year cycle for RDL2 and RDL3, a 36-year cycle for RDL4 and RDL5, and a 14-year cycle (RDL6), becoming more frequent during modern warming.
- Our detrital proxies suggest that the two arms of Mittie Glacier exhibit distinct behaviors: following a 14-year cycle, a subglacial channel transports water from the sudden release of a large subglacial lake ($\sim 4 \text{ km}^3$; Gray et al., 2024) at the glacier front, inducing hyperpycnal events downstream of the western arm, while the eastern arm is undergoing surges.

Acknowledgements. Some of the data presented herein were collected by the Canadian research icebreaker CCGS Amundsen and

made available by the Amundsen Science program, which is supported by the Canada Foundation for Innovation Major Science Initiatives Fund. We would like to thank the captain, officers, crew, and scientists onboard the CCGS Amundsen during the 2021 (Leg 3) ArcticNet expedition for the acquisition of swath-bathymetric data and the recovery of the sediment cores used in this study. We also thank Quentin Beauvais (ISMER-UQAR) for his help with X-CT scans and Multi-Sensor Core Logger analysis; Claude Belzile (ISMER-UQAR) for his advice with the grain size analyses; Antonin Prijac and Nicole Sanderson (Geotop-UQAM) for their advice on the ^{210}Pb measurements; and Nicolas Van Nieuwenhove (University of New Brunswick) for the foraminifera picking. Finally, we thank Matt O'Regan (Stockholm University) and an anonymous reviewer for their constructive reviews, which significantly improved the quality of the manuscript. We also thank Mary Edwards for her editorial support. This research was funded by ArcticNet (a Network of Centers of Excellence Canada), Amundsen Science, Geotop, Québec-Océan, the Natural Sciences and Engineering Research Council of Canada (NSERC) through Discovery grants to J.-C. Montero-Serrano, G. St-Onge, P. Lajeunesse, and L. Copland, and the ISMER excellence scholarship and PBEEE-FRQNT scholarship N°350396 (<https://doi.org/10.69777/350396>) provided to Élodie Bracquart.

Conflict of interest—The authors declare no conflicts of interest.

Data Availability Statement

All analytical data presented will be available electronically in the PANGAEA database (<https://www.pangaea.de/>). Maps were made using ArcGIS Pro software version 3.1.3, figures using Golden Software Grapher 24, and the age-depth models using the R Plum package version 4.4.2.

Supporting information

Additional supporting information may be found in the online version of this article at the publisher's website.

Figure S1. (A) Core top correlations of the k_{LF} and b^* profiles of cores 22BC, 01TWC and 01PC used to create the 01SBCS composite sequence. (B) core top correlations of the k_{LF} and $\ln(\text{Fe}/\text{Ca})$ profiles of cores 23BC and 01GC used to create the 01MCS composite sequence.

Figure S2. (A, C, E, G) Sortable silt mean size (\overline{SS}) vs percentage of sortable silt ($SS\%$). (B, D, F, H) \overline{SS} and the running five-point correlation profiles. The grey areas indicate sections of the sortable silt record that do not pass the reliability test of a downcore correlation coefficient > 0.5 between \overline{SS} and $SS\%$ (McCave and Andrews, 2019b).

Figure S3. X-CT scan image, high-resolution core photography and associated lithofacies for cores 22BC and 01PC studied here.

Figure S4. X-CT scan image, high-resolution core photography and associated lithofacies for cores 23BC and 01GC studied here.

Figure S5. High-resolution core photography, X-CT image, magnetic susceptibility (k_{LF}), D_{90} (μm), $\ln(\text{Zr}/\text{Rb})$, ^{210}Pb activity, ^{210}Pb excess, ^{210}Pb excess without the RDL layers, age (CE) for the composite cores.

Table S1. ^{210}Pb measurements.

References

- Amundsen Science. (2008) *2008 CCGS Amundsen expedition report*. Québec: Amundsen Science. Available from: <https://amundsenscience.com/expeditions/2007-2008-expedition/> [Retrieved 5th February 2025].
- Amundsen Science. (2021) *2021 CCGS Amundsen expedition report*. Québec: Amundsen Science. Available from: <https://amundsenscience.com/expeditions/2021-expedition/> [Retrieved 5th February 2025].

- Andrews, J.T. & Eberl, D.D. (2012) Determination of sediment provenance by unmixing the mineralogy of source-area sediments: the "SedUnMix" program. *Marine Geology*, 291–294, 24–33. Available from: <https://doi.org/10.1016/j.margeo.2011.10.007>
- Andrews, J.T., Björk, A.A., Eberl, D.D., Jennings, A.E. & Verplanck, E.P. (2015) Significant differences in late Quaternary bedrock erosion and transport: East versus West Greenland ~ 70° N—evidence from the mineralogy of offshore glacial marine sediments. *Journal of Quaternary Science*, 30, 452–463. Available from: <https://doi.org/10.1002/jqs.2787>
- Andrews, J.T., Klein, A.J., Jenner, K.A., Jennings, A.E. & Campbell, C. (2018) The variability of Baffin Bay seafloor sediment mineralogy: the identification of discrete glacial sediment sources and application to Late Quaternary downcore analysis. *Canadian Journal of Earth Sciences*, 55(6), 620–639. Available from: <https://doi.org/10.1139/cjes-2017-0223>
- Andrews, J.T., Stein, R., Moros, M. & Perner, K. (2016) Late Quaternary changes in sediment composition on the NE Greenland margin (~73° N) with a focus on the fjords and shelf. *Boreas*, 45, 381–397. Available from: <https://doi.org/10.1111/bor.12169>
- Bader, J., Jungclauss, J., Krivova, N., Lorenz, S., Maycock, A., Raddatz, T., et al. (2020) Global temperature modes shed light on the Holocene temperature conundrum. *Nature Communications*, 11(1), 4726. Available from: <https://doi.org/10.1038/s41467-020-18478-6>
- Bailey, J. N.-L., Macdonald, R. W., Sanei, H., Outridge, P. M., Johannessen, S. C., Hochheim, K., et al. (2013) Change at the margin of the North Water Polynya, Baffin Bay, inferred from organic matter records in dated sediment cores. *Marine Geology*, 341, 1–13. Available from: <https://doi.org/10.1016/j.margeo.2013.04.017>
- Belzile, C. & Montero-Serrano, J.-C. (2022) Quantifying simulated fine sand fraction in muddy sediment using laser diffraction. *Canadian Journal of Earth Sciences*, 59(7), 455–461. Available from: <https://doi.org/10.1139/cjes-2022-0011>
- Bicera-Nfundiko, C. (2024) *Comparaison des environnements sédimentaires à proximité des glaciers Humboldt (Groenland) et Eugénie-Dobbin (île d'Ellesmere)*. Mémoire. Rimouski: Université du Québec à Rimouski, Institut des sciences de la mer (ISMER), 122 p.
- Blaauw, M. & Christen, J.A. (2011) Flexible paleoclimate age–depth models using an autoregressive gamma process. *Bayesian Analysis*, 6, 457–474. Available from: <https://doi.org/10.1214/11-BA618>
- Blake Jr., W. (1993) Holocene emergence along the Ellesmere Island coasts of northernmost Baffin Bay. *Norsk geologisk tidsskrift*, 73(3), 147–160.
- Blott, S.J. & Pye, K. (2001) GRADISTAT: a grain size distribution and statistics package for the analysis of unconsolidated sediments. *Earth Surface Processes and Landforms*, 26, 1237–1248. Available from: <https://doi.org/10.1002/esp.261>
- Bouma, A.H. (1962) *Sedimentology of some flysch deposits. A graphic approach to facies interpretation*. Amsterdam: Elsevier.
- Briner, J.P., Davis, P.T. & Miller, G.H. (2009) Latest Pleistocene and Holocene glaciation of Baffin Island, arctic Canada: key patterns and chronologies. *Quaternary Science Reviews*, 28, 2075–2087. Available from: <https://doi.org/10.1016/j.quascirev.2008.09.017>
- Briner, J.P., McKay, N.P., Axford, Y., Bennike, O., Bradley, R.S., de Vernal, A., et al. (2016) Holocene climate change in Arctic Canada and Greenland. *Quaternary Science Reviews*, 147, 340–364. Available from: <https://doi.org/10.1016/j.quascirev.2016.02.010>
- Brown, R.J.E. (1972) Permafrost in the Canadian Arctic Archipelago. *Zeitschrift für Geomorphologie*, 13, 102–130.
- Bruel, R. & Sabatier, P. (2020) serac: an R package for ShortlivEd RAdionuclide chronology of recent sediment cores. *Journal of Environmental Radioactivity*, 225, 106449. Available from: <https://doi.org/10.1016/j.jenvrad.2020.106449>
- Buizert, C., Keisling, B.A., Box, J.E., He, F., Carlson, A.E., Sinclair, G. et al. (2018) Greenland-wide seasonal temperatures during the last deglaciation. *Geophysical Research Letters*, 45(4), 1905–1914. Available from: <https://doi.org/10.1002/2017GL075601>
- Butler, B. & Hillier, S. (2021) powdR: an R package for quantitative mineralogy using full pattern summation of X-ray powder diffraction data. *Computers & Geosciences*, 147, 104662. Available from: <https://doi.org/10.1016/j.cageo.2020.104662>
- Caron, M., Montero-Serrano, J. C., St-Onge, G. & Rochon, A. (2020) Quantifying provenance and transport pathways of Holocene sediments from the northwestern Greenland margin. *Paleoceanography and Paleoclimatology*, 34, e2019PA003809. Available from: <https://doi.org/10.1029/2019PA003809>
- Caron, M., Rochon, A., Montero-Serrano, J.C. & St-Onge, G. (2019) Evolution of sea-surface conditions on the northwestern Greenland margin during the Holocene. *Journal of Quaternary Science*, 34, 569e580. Available from: <https://doi.org/10.1002/jqs.3146>
- Carr, J.R., Stokes, C.R. & Vieli, A. (2013) Recent progress in understanding marine-terminating Arctic outlet glacier response to climatic and oceanic forcing: twenty years of rapid change. *Progress in Physical Geography: Earth and Environment*, 37(4), 436–467. Available from: <https://doi.org/10.1177/0309133313483163>
- Ciraci, E., Velicogna, I., & Swenson, S. (2020) Continuity of the mass loss of the world's glaciers and ice caps from the GRACE and GRACE Follow-On missions. *Geophysical Research Letters*, 47(9), e2019GL086926. Available from: <https://doi.org/10.1029/2019GL086926>
- Cohen, J., Screen, J. A., Furtado, J. C., Barlow, M., Whittleston, D., Coumou, D., et al. (2014) Recent Arctic amplification and extreme mid-latitude weather. *Nature Geoscience*, 7(9), 627–637. Available from: <https://doi.org/10.1038/ngeo2234>
- Cook, A.J., Copland, L., Noël, B.P.Y., Stokes, C.R., Bentley, M.J., Sharp, M.J., et al. (2019) Atmospheric forcing of rapid marine-terminating glacier retreat in the Canadian Arctic Archipelago. *Science Advances*, 5, eaau8507. Available from: <https://doi.org/10.1126/sciadv.aau8507>
- Copland, L., Halle, D., Van Wychen, W., Lauzon, B., Dowdeswell, J.A. & Davis, J. (2024) Characteristics of the 15-year surge of Mittie Glacier, SE Ellesmere Island, Canadian Arctic. *Annals of Glaciology*, 65, 1–13. Available from: <https://doi.org/10.1017/aog.2024.31>
- Copland, L., Sharp, M.J. & Dowdeswell, J.A. (2003) The distribution and flow characteristics of surge-type glaciers in the Canadian High Arctic. *Annals of Glaciology*, 36, 73–81. Available from: <https://doi.org/10.3189/172756403781816301>
- Dalton, A., Copland, L., Tivy, A., Van Wychen, W. & Cook, A. (2019) Iceberg production and characteristics around the Prince of Wales Icefield, Ellesmere Island, 1997–2015. *Arctic, Antarctic, and Alpine Research*, 51(1), 412–427. Available from: <https://doi.org/10.1080/15230430.2019.1634442>
- Dalton, A.S., Margold, M., Stokes, C.R., Tarasov L., Dyke A.S., Adams R.S., et al. (2020) An updated radiocarbon-based ice margin chronology for the last deglaciation of the North American Ice Sheet Complex. *Quaternary Science Reviews*, 234, 106223. Available from: <https://doi.org/10.1016/j.quascirev.2020.106223>
- Debret, M., Sebag, D., Desmet, M., Balsam, W., Copard, Y., Mourier, B., et al. (2011) Spectrocolorimetric interpretation of sedimentary dynamics: the new "Q7/4 diagram". *Earth-Science Reviews*, 109(1–2), 1–19. Available from: <https://doi.org/10.1016/j.earscirev.2011.07.002>
- Dowdeswell, J.A., Hamilton, G.S. & Hagen, J.O. (1991) The duration of the active phase on surge-type glaciers: contrasts between Svalbard and other regions. *Journal of Glaciology*, 37(127), 388–400. Available from: <https://doi.org/10.3189/S00222143000005827>
- Dowdeswell, J.A., Hogan, K.A., Arnold, N.S., Mugford, R.I., Wells, M., Hirst, J.P.P., et al. (2015) Sediment-rich meltwater plumes and ice-proximal fans at the margins of modern and ancient tidewater glaciers: observations and modelling. *Sedimentology*, 62(6), 1665–1692. Available from: <https://doi.org/10.1111/sed.12198>
- Dunphy, M., Dupont, F., Hannah, C.G. & Greenberg, D. (2005) *Validation of a modelling system for tides in the Canadian Arctic Archipelago*. Maritimes Region: Fisheries & Oceans Canada, Ocean Sciences Division, Bedford Institute of Oceanography.
- Dyke, A.S., Andrews, J.T., Clark, P.U., England, J.H., Miller, G.H., Shaw, J. et al. (2002) The Laurentide and Innuitian ice sheets during the last glacial maximum. *Quaternary Science Reviews*, 21 (1–3), 9–31. Available from: [https://doi.org/10.1016/S0277-3791\(01\)00095-6](https://doi.org/10.1016/S0277-3791(01)00095-6)
- Eberl, D.D. (2003) User's guide to RockJock—A program for determining quantitative mineralogy from powder X-ray diffraction data. *U.S. Geological Survey Open-File Report*, 2003-78, 47 p. Available from: <https://doi.org/10.3133/ofr200378>
- England, J., Atkinson, J., Bednarski, J., Dyke, A.S., Hodgson, D.A. & Ó Cofaigh, C. (2006) The Innuitian Ice Sheet: configuration, dynamics and chronology. *Quaternary Science Reviews*, 25, 689e703. Available from: <https://doi.org/10.1016/j.quascirev.2005.08.007>

- Georgiadis, E., Giraudeau, J., Martinez, P., Lajeunesse, P., St-Onge, G., Schmidt, S. et al. (2018) Deglacial to postglacial history of Nares Strait, Northwest Greenland: a marine perspective from Kane Basin. *Climate of the Past*, 14, 1991–2010. Available from: <https://doi.org/10.5194/cp-14-1991-2018>
- Ghaleb, B. (2009) Overview of the methods for the measurement and interpretation of short-lived radioisotopes and their limits. *IOP conference series: Earth and environmental science*, 5(1), 012007. Available from: <https://doi.org/10.1088/1755-1307/5/1/012007>
- Gray, L., Lauzon, B., Copland, L., Van Wychen, W., Dow, C., Kochtitzky, W. et al. (2024) Tracking the filling, outburst flood and resulting subglacial water channel from a large Canadian Arctic subglacial lake. *Geophysical Research Letters*, 51(19), e2024GL110456. Available from: <https://doi.org/10.1029/2024GL110456>
- Grobe, H. (1987) A simple method for the determination of ice-rafted debris in sediment cores. *Polarforschung*, 57, 123–126.
- Grove, J.M. (1988) *The little ice age*. London: Methuen.
- Harrison, J.C., Thorsteinsson, R., Frisch, T., Mayr, U., Gilbert, C., Lynds, T. et al. (2015) Geology, Tectonic assemblage map of Grise Fiord, eastern Devon and southern Ellesmere islands, Nunavut; Geological Survey of Canada, Canadian Geoscience Map 34 (2nd edition, preliminary), scale 1:500 000. Ottawa, ON: Natural Resources Canada. Available from: <https://doi.org/10.4095/296222>
- Heaton, T.J., Köhler, P., Butzin, M., Bard E., Reimer R.W., Austin W.E.N., et al. (2020) Marine20—The marine radiocarbon age calibration curve (0–55,000 cal BP). *Radiocarbon*, 62(4), 779–820. Available from: <https://doi.org/10.1017/RDC.2020.68>
- Hiscott, R.N., Aksu, A.E. & Nielsen, O.B. (1989) Provenance and dispersal patterns, Pliocene-Pleistocene section at site 645, Baffin Bay. *Proceedings of the Ocean Drilling Program, Scientific Results*, 105, 31–52. Available from: <https://doi.org/10.2973/odp.proc.sr.105.117.1989>
- Huang, J., Zhang, X., Zhang, Q., Lin, Y., Hao, M., Luo, Y., et al. (2017) Recently amplified arctic warming has contributed to a continual global warming trend. *Nature Climate Change*, 7(12), 875–879. Available from: <https://doi.org/10.1038/s41558-017-0009-5>
- IPCC. (2021) *Climate change 2021: The physical science basis. Contribution of working group I to the sixth assessment report of the intergovernmental panel on climate change* [Masson-Delmotte, V., Zhai, P., Pirani, A., Connors, S.L., Péan, C. & Berger, S., et al. (Eds.)]. Cambridge, UK; New York, NY, USA: Cambridge University Press. Available from: <https://doi.org/10.1017/9781009157896>
- Jackson, R., Kvorning, A.B., Limoges, A., Georgiadis, E., Olsen, S. M., Tallberg, P., et al. (2021) Holocene polynya dynamics and their interaction with oceanic heat transport in northernmost Baffin Bay. *Scientific Reports*, 11, 10095. Available from: <https://doi.org/10.1038/s41598-021-88517-9>
- Jakobsson, M., Mayer, L.A., Bringenspar, C., Castro C.F., Mohammad R., Johnson P., et al. 2020 The International Bathymetric chart of the Arctic Ocean version 4.0. *Scientific Data*, 7, 176. Available from: <https://doi.org/10.1038/s41597-020-0520-9>
- Jennings, A., Reilly, B., Andrews, J., Hogan, K., Walczak, M., Jakobsson, M., et al. (2022) Modern and early Holocene ice shelf sediment facies from Petermann Fjord and northern Nares Strait, northwest Greenland. *Quaternary Science Reviews*, 283, 107460. Available from: <https://doi.org/10.1016/j.quascirev.2022.107460>
- Jennings, A., Sheldon, C., Cronin, T., Francus, P., Stoner, J. & Andrews, J. (2011) The Holocene History of Nares Strait: transition from glacial bay to Arctic–Atlantic throughflow. *Oceanography*, 24, 26–41. Available from: <https://doi.org/10.5670/oceanog.2011.52>
- Jennings, A.E., Andrews, J.T., Oliver, B., Walczak, M. & Mix, A. (2019) Retreat of the smith sound ice stream in the early Holocene. *Boreas*, 48, 825–840. Available from: <https://doi.org/10.1111/bor.12391>
- Jennings, A.E., Andrews, J.T., Ó Cofaigh, C., St-Onge, G., Sheldon, C., Belt, S.T., et al. (2017) Ocean forcing of Ice Sheet retreat in central west Greenland from LGM to the early Holocene. *Earth and Planetary Science Letters*, 472, 1–13. Available from: <https://doi.org/10.1016/j.epsl.2017.05.007>
- Jennings, A.E., Walton, M.E., Ó Cofaigh, C., Kilfeather, A., Andrews, J.T., Ortiz, J.D., et al. (2014) Paleoenvironments during Younger Dryas–Early Holocene retreat of the Greenland Ice Sheet from outer Disko Trough, central west Greenland. *Journal of Quaternary Science*, 29(1), 27–40. Available from: <https://doi.org/10.1002/jqs.2652>
- Jiskoot, H., Boyle, P. & Murray, T. (1998) The incidence of glacier surging in Svalbard: evidence from multivariate statistics. *Computers & Geosciences*, 24(4), 387–399. Available from: [https://doi.org/10.1016/S0098-3004\(98\)00033-8](https://doi.org/10.1016/S0098-3004(98)00033-8)
- Jones, P.D. & Mann, M.E. (2004) Climate over past millennia. *Reviews of Geophysics*, 42, RG2002. Available from: <https://doi.org/10.1029/2003RG000143>
- Kaufman, D., Ager, T.A., Anderson, N.J., Anderson, P.M., Andrews, J.T. & Bartlein, P.J. et al. (2004) Holocene thermal maximum in the western Arctic (0–180° W). *Quaternary Science Reviews*, 23(5–6), 529–560. Available from: <https://doi.org/10.1016/j.quascirev.2003.09.007>
- Kaufman, D.S., Schneider, D.P., McKay, N.P., Ammann C.M., Bradley R.S., Briffa K.R., et al. (2009) Recent warming reverses long-term Arctic cooling. *Science*, 325(5945), 1236–1239. Available from: <https://doi.org/10.1126/science.1173983>
- Kelleher, R., Jennings, A., Andrews, J., Brooks, N.K.S., Marchitto, T., Feng, S., et al. (2022) Late glacial retreat of the Lancaster Sound Ice Stream and early Holocene onset of Arctic/Atlantic throughflow in the Arctic Island channels. *Arctic, Antarctic, and Alpine Research*, 54(1), 395–427. Available from: <https://doi.org/10.1080/15230430.2022.2110689>
- Knudsen, K.L., Stabell, B., Seidenkrantz, M.-S., Eiríksson, J. & Blake, W. (2008) Deglacial and Holocene conditions in northernmost Baffin Bay: sediments, foraminifera, diatoms and stable isotopes. *Boreas*, 37, 346e376. Available from: <https://doi.org/10.1111/j.1502-3885.2008.00035.x>
- Kochtitzky, W. & Copland, L. (2022) Retreat of Northern Hemisphere marine-terminating glaciers, 2000–2020. *Geophysical Research Letters*, 49(3), e2021GL096501. Available from: <https://doi.org/10.1029/2021GL096501>
- Laskar, J., Robutel, P., Joutel, F., Gastineau, M., Correia, A.C.M. & Levrard, B. (2004) A long-term numerical solution for the insolation quantities of the Earth. *Astronomy & Astrophysics*, 428, 261e285. Available from: <https://doi.org/10.1051/0004-6361:20041335>
- Lecavalier, B.S., Fisher, D.A., Milne, G.A., Vinther, B. M., Tarasov, L., Huybrechts, P., et al. (2017) High Arctic Holocene temperature record from the Agassiz ice cap and Greenland ice sheet evolution. *Proceedings of the National Academy of Sciences*, 114, 5952–5957. Available from: <https://doi.org/10.1073/pnas.1616287114>
- Marcott S.A., Shakun J.D., Clark P.U. & Mix, A.C. (2013) A reconstruction of regional and global temperature for the past 11,300 years. *Science*, 339(6124), 1198–1201. Available from: <https://doi.org/10.5194/wcd-6-43-2025>
- Marlowe, J.I. (1966) Mineralogy as an indicator of long-term current fluctuations in Baffin Bay. *Canadian Journal of Earth Sciences*, 3(2), 191–201. Available from: <https://doi.org/10.1139/e66-015>
- Mayewski, P.A., Rohling, E.E., Curt Stager, J., Karlén W., Maasch K.A., Meeker L.D., et al. (2004) Holocene climate variability. *Quaternary Research*, 62(3), 243–255. Available from: <https://doi.org/10.1016/j.yqres.2004.07.001>
- McCave, I.N. & Andrews, J.T. (2019a) Distinguishing current effects in sediments delivered to the ocean by ice. I. Principles, methods and examples. *Quaternary Science Reviews*, 212, 92–107. Available from: <https://doi.org/10.1016/j.quascirev.2019.03.031>
- McCave, I.N. & Andrews, J. T. (2019b) Distinguishing current effects in sediments delivered to the ocean by ice. II. Glacial to Holocene changes in high latitude North Atlantic upper ocean flows. *Quaternary Science Reviews*, 223, 105902. Available from: <https://doi.org/10.1016/j.quascirev.2019.105902>
- McKay, N.P., Kaufman, D.S., Routson, C.C., Erb, M.P. & Zander, P.D. (2018) The onset and rate of Holocene Neoglacial cooling in the Arctic. *Geophysical Research Letters*, 45, 12487–12496. Available from: <https://doi.org/10.1029/2018GL079773>
- Meier, M.F. & Post, A. (1969) What are glacier surges? *Canadian Journal of Earth Sciences*, 6(4), 807–817. Available from: <https://doi.org/10.1139/e69-081>
- Miller, G.H., Geirsdóttir, Á., Zhong, Y., Larsen, D.J., Otto-Bliesner, B.L. & Holland, M.M., et al. (2012) Abrupt onset of the Little Ice Age triggered by volcanism and sustained by sea-ice/ocean feedbacks. *Geophysical Research Letters*, 39(2), 2708. Available from: <https://doi.org/10.1029/2011GL050168>

- Miller, G.H., Wolfe, A.P., Briner, J.P., Sauer, P.E. & Nesje, A. (2005) Holocene glaciation and climate evolution of Baffin Island, Arctic Canada. *Quaternary Science Reviews*, 24, 1703–1721. Available from: <https://doi.org/10.1016/j.quascirev.2004.06.021>
- Mulder, T., Syvitski, J.P.M., Migeon, S., Faugères, J.C. & Savoye, B. (2003) Marine hyperpycnal flows: initiation, behavior and related deposits. A review. *Marine and Petroleum Geology*, 20, 861–882. Available from: <https://doi.org/10.1016/j.marpetgeo.2003.01.003>
- Noël, B., van de Berg, W.J., Lhermitte, S., Wouters, B., Schaffer, N. & van den Broeke, M.R. (2018) Six decades of glacial mass loss in the Canadian Arctic Archipelago. *Journal of Geophysical Research: Earth Surface*, 123, 1430–1449. Available from: <https://doi.org/10.1029/2017JF004304>
- Ó Cofaigh, C., Taylor, J., Dowdeswell, J.A. & Pudsey, C.J. (2003) Palaeo-ice streams, trough mouth fans and high-latitude continental slope sedimentation. *Boreas*, 32(1), 37–55. Available from: <https://doi.org/10.1080/03009480310001858>
- Okuma, E., Hingst, J., Weiser, J., Madaj, L., Titschack, J., Vogt, C., et al. (2023) Deglacial and Holocene sediment dynamics and provenances off Lancaster Sound: implications for paleoenvironmental conditions in northern Baffin Bay. *Quaternary Science Reviews*, 309, 108101. Available from: <https://doi.org/10.1016/j.quascirev.2023.108101>
- Omotoso, O., McCarty, D.K., Hillier, S. & Kleeberg, R. (2006) Some successful approaches to quantitative mineral analysis as revealed by the 3rd Reynolds Cup contest. *Clays and Clay Minerals*, 54(6), 748–760. Available from: <https://doi.org/10.1346/CCMN.2006.0540609>
- O'Regan, M., Cronin, T. M., Reilly, B., Alstrup A.K.O., Gemery L., Golub A., et al. (2021) The Holocene dynamics of Ryder Glacier and ice tongue in north Greenland. *The Cryosphere*, 15(8), 4073–4097. Available from: <https://doi.org/10.5194/tc-15-4073-2021>
- Pearce, C., Özdemir, K.S., Forchhammer Mathiasen, R., Detlef, H., and Olsen, J. (2023) The marine reservoir age of Greenland coastal waters. *Geochronology*, 5, 451–465. Available from: <https://doi.org/10.5194/gchron-5-451-2023>
- Pieńkowski, A.J., England, J.H., Furze, M.F.A., Blasco, S., Mudie, P.J. & MacLean, B. (2013) 11,000 yrs of environmental change in the Northwest passage: a multiproxy core record from central Parry Channel, Canadian High Arctic. *Marine Geology*, 341, 68–85. Available from: <https://doi.org/10.1016/j.margeo.2013.04.008>
- Pieńkowski, A.J., England, J.H., Furze, M.F.A., Marret, F., Eynaud, F., Vilks, G., et al. (2012) The deglacial to postglacial marine environments of SE Barrow Strait, Canadian Arctic Archipelago. *Boreas*, 41, 141–179. Available from: <https://doi.org/10.1111/j.1502-3885.2011.00227.x>
- Powell, R.D. (1981) A model for sedimentation by tidewater glaciers. *Annals of Glaciology*, 2, 129–134. Available from: <https://doi.org/10.3189/172756481794352306>
- Raymond, C.F. (1987) How do glaciers surge? A review. *Journal of Geophysical Research: Solid Earth*, 92(B9), 9121–9134. Available from: <https://doi.org/10.1029/JB092iB09p09121>
- Renssen, H., Seppä, H., Crosta, X., Goosse, H. & Roche, D.M. (2012) Global characterization of the Holocene thermal maximum. *Quaternary Science Reviews*, 48, 7–19. Available from: <https://doi.org/10.1016/j.quascirev.2012.05.022>
- Ribeiro, S., Limoges, A., Massé, G., Johansen K.L., Colgan W., Weckström K., et al. (2021) Vulnerability of the NorthWater ecosystem to climate change. *Nature Communications*, 12, 4475. Available from: <https://doi.org/10.1038/s41467-021-24742-0>
- Rodríguez-Cuicas, M. E., Montero-Serrano, J.C., St-Onge, G. & Normandeau, A. (2023) A 600-year marine record associated with the dynamics of the eastern Penny Ice Cap (Baffin Island, Nunavut, Canada). *Journal of Quaternary Science*, 38(7), 1062–1081. Available from: <https://doi.org/10.1002/jqs.3531>
- Sadler, H.E. (1973) On the oceanography of Makinson inlet. *Arctic*, 26(1), 76–77. Available from: <https://www.jstor.org/stable/40508357>
- Serreze, M.C. & Barry, R.G. (2011) Processes and impacts of Arctic amplification: a research synthesis. *Global and Planetary Change*, 77(1–2), 85–96. Available from: <https://doi.org/10.1016/j.gloplacha.2011.03.004>
- Serreze, M.C. & Francis, J.A. (2006) The Arctic amplification debate. *Climatic Change*, 76(3), 241–264. Available from: <https://doi.org/10.1007/s10584-005-9017-y>
- Sevestre, H. & Benn, D.I. (2015) Climatic and geometric controls on the global distribution of surge-type glaciers: implications for a unifying model of surging. *Journal of Glaciology*, 61(228), 646–662. Available from: <https://doi.org/10.3189/2015JoG14136>
- Sharp, M., Burgess, D.O., Cawkwell, F., Copland, L., Davis, J.A. & Dowdeswell, E.K. et al. (2014) Remote sensing of recent glacier changes in the Canadian Arctic. In: Kargel, J.S., Leonard, G. J., Bishop, M.P., Kääb, A. & Raup, B.H. (Eds.) *Global land ice measurements from space*, Chapter 9, Berlin, Heidelberg: Springer Praxis Books, pp. 205–228. Available from: https://doi.org/10.1007/978-3-540-79818-7_9
- Sharp, M., Burgess, D.O., Cogley, J.G., Ecclestone, M., Labine, C. & Wolken, G.J. (2011) Extreme melt on Canada's Arctic ice caps in the 21st century. *Geophysical Research Letters*, 38(11). Available from: <https://doi.org/10.1029/2011GL047381>
- Short, N.H. & Gray, A.L. (2005) Glacier dynamics in the Canadian High Arctic from RADARSAT-1 speckle tracking. *Canadian Journal of Remote Sensing*, 31(3), 225–239. Available from: <https://doi.org/10.5589/m05-010>
- Simon, Q., Hillaire-Marcel, C., St-Onge, G. & Andrews, J.T. (2014) North-eastern Laurentide, western Greenland and southern Inuitian ice stream dynamics during the last glacial cycle. *Journal of Quaternary Science*, 29(1), 14–26. Available from: <https://doi.org/10.1002/jqs.2648>
- Solomina, O.N., Bradley, R.S., Hodgson, D.A., Ivy-Ochs, S., Jomelli, V., Mackintosh, A.N., et al. (2015) Holocene glacier fluctuations. *Quaternary Science Reviews*, 111, 9–34. Available from: <https://doi.org/10.1016/j.quascirev.2014.11.018>
- Stevenard, N., Montero-Serrano, J.C., Eynaud, F., St-Onge, G., Zaragosi, S. & Copland, L. (2022) Lateglacial and Holocene sedimentary dynamics in northwestern Baffin Bay as recorded in sediment cores from Cape Norton Shaw Inlet (Nunavut, Canada). *Boreas*, 51(3), 532–552. Available from: <https://doi.org/10.1111/bor.12575>
- St-Onge, M.P. & St-Onge, G. (2014) Environmental changes in Baffin Bay during the Holocene based on the physical and magnetic properties of sediment cores. *Journal of Quaternary Science*, 29, 41–56. Available from: <https://doi.org/10.1002/jqs.2674>
- St-Onge, G., Mulder, T., Francus, P. & Long, B. (2007) Continuous physical properties of cored marine sediments. In: Hillaire-Marcel, C. & de Vernal, A. (Eds.) *Proxies in Late Cenozoic paleoceanography*. Development in Marine Geology, 1:63–98. Available from: [https://doi.org/10.1016/S1572-5480\(07\)01007-X](https://doi.org/10.1016/S1572-5480(07)01007-X)
- Tang, C.C.L., Ross, C.K., Yao, T., Petrie, B., DeTracey, B.M. & Dunlap, E. (2004) The circulation, water masses and sea-ice of Baffin Bay. *Progress in Oceanography*, 63, 183–228. Available from: <https://doi.org/10.1016/j.pocan.2004.09.005>
- Thomson, L.I., Osinski, G.R. & Ommanney, C.S.L. (2011) Glacier change on Axel Heiberg Island, Nunavut, Canada. *Journal of Glaciology*, 57(206), 1079–1086. Available from: <https://doi.org/10.3189/002214311798843287>
- Vincent, R.F. & Marsden, R.F. (2008) A study of tidal influences in the North Water polynya using short time span satellite imagery. *Arctic*, 61(4), 373–380. <https://doi.org/10.14430/arctic45>
- Van Wychen, W., Burgess, D. O., Gray, L., Copland, L., Sharp, M., Dowdeswell, J. A. et al. (2014) Glacier velocities and dynamic ice discharge from the Queen Elizabeth Islands, Nunavut, Canada. *Geophysical Research Letters*, 41(2), 484–490. Available from: <https://doi.org/10.1002/2013GL058558>
- Van Wychen, W., Burgess, D., Kochtitzky, W., Nikolic, N., Copland, L. & Gray, L. (2020) RADARSAT-2 derived glacier velocities and dynamic discharge estimates for the Canadian high arctic: 2015–2020. *Canadian Journal of Remote Sensing*, 46(6), 695–714. Available from: <https://doi.org/10.1080/07038992.2020.1859359>
- Van Wychen, W., Davis, J., Burgess, D. O., Copland, L., Gray, L., Sharp, M. et al. (2016) Characterizing interannual variability of glacier dynamics and dynamic discharge (1999–2015) for the ice masses of Ellesmere and Axel Heiberg

- Islands, Nunavut, Canada. *Journal of Geophysical Research: Earth Surface*, 121(1), 39–63. Available from: <https://doi.org/10.1002/2015JF003708>
- Wanner, H., Beer, J., Bütikofer, J., Crowley T.J., Cubasch U., Flückiger J., et al. (2008) Mid- to Late Holocene climate change: an overview. *Quaternary Science Reviews*, 27, 1791–1828. Available from: <https://doi.org/10.1016/j.quascirev.2008.06.013>
- White, A. & Copland, L. (2018) Area change of glaciers across Northern Ellesmere Island, Nunavut, between ~1999 and ~2015. *Journal of Glaciology*, 64(246), 609–623. Available from: <https://doi.org/10.1017/jog.2018.49>
- Zavala, C. (2020) Hyperpycnal (over density) flows and deposits. *Journal of Palaeogeography*, 9(1), 1–21. Available from: <https://doi.org/10.1186/s42501-020-00065-x>